

Olivier Marchal

Optimal estimation of atmospheric ^{14}C production over the Holocene: paleoclimate implications

Received: 16 December 2003 / Accepted: 27 August 2004 / Published online: 19 November 2004
© Springer-Verlag 2004

Abstract A tree-ring $\Delta^{14}\text{C}$ record and a simple box model of the global ^{14}C cycle are combined using a method of optimal estimation theory (Rauch-Tung-Striebel smoother). The combination is used to infer information about the time evolution of ^{14}C production in the atmosphere (\mathcal{P}) for the period 9400 year BC to AD 1900 year. Unlike previous attempts to infer \mathcal{P} changes from the tree-ring record, the errors in both the $\Delta^{14}\text{C}$ data and the model, which are assumed to be purely random (not systematic), are formally considered. The optimal time evolution of \mathcal{P} is compared to independent evidence of changes in cosmogenic nuclide production over the Holocene from a variety of records on their original chronology, e.g., a record of the virtual axial dipole moment (VADM) based on a compilation of archeomagnetic data, the record of ^{10}Be concentration from the GISP2 ice core (Central Greenland), and the record of ^{10}Be concentration from the PS1 ice core (South Pole). The rank correlations between \mathcal{P} -VADM, \mathcal{P} - ^{10}Be (GISP2), and \mathcal{P} - ^{10}Be (PS1) are highly significant ($p < 0.01$), indicating that geomagnetic field intensity and ^{10}Be concentration in GISP2 and PS1 changed monotonically with ^{14}C production. The linear correlation coefficients between \mathcal{P} -VADM, \mathcal{P} - ^{10}Be (GISP2), and \mathcal{P} - ^{10}Be (PS1) are also highly significant ($p < 0.01$) but relatively small (-0.76 , 0.48 , and 0.60 , respectively). Thus, an important fraction (42–77%) of the variance in the geomagnetic and ^{10}Be data is not accounted for by linear regression on the ^{14}C productions implied by the tree-ring record. The \mathcal{P} variance near the 1500 yr period, which previous

authors interpreted as solar variability, represents a small fraction of the total variance in the \mathcal{P} time series ($<15\%$ for the band 1200–1800 yr) and does not correspond to a spectral peak. Hence, the hypothesis of a direct solar forcing mechanism for the postulated millennial climate variability during the Holocene is not supported.

1 Introduction

The measurements of ^{14}C concentration on dendrochronologically dated wood samples ($\Delta^{14}\text{C}$, corrected for fractionation effects) probably provide one of the most accurate records in paleoclimatology (e.g., Stuiver et al. 1998). One important application of the tree-ring $\Delta^{14}\text{C}$ record is the estimation of the changes in atmospheric ^{14}C production (\mathcal{P} hereafter) over the Holocene (e.g., Stuiver and Braziunas 1989, 1993a, b; Stuiver et al. 1991; Bond et al. 2001). Previous studies interpreted tree ring-based \mathcal{P} “oscillations” on the centennial scale (e.g., Stuiver and Braziunas 1989) and millennial scale (Bond et al. 2001) in terms of changes in solar activity. If this interpretation is correct, these variations may be relevant to the study of both solar physics and earth paleoclimates. In particular, they were used to support the hypothesis that a solar forcing mechanism was responsible for the postulated millennial climate variability during the Holocene (Bond et al. 2001). Climate variability at this time scale is difficult to rationalize, as the millennial frequency occurs near the middle of a wide gap in the spectrum of external (orbital) forcing (Munk et al. 2000). The important question is thus whether solar forcing is responsible for the presence of one or several peaks in the orbital gap.

In spite of their importance, almost no attention seems to have been paid to the uncertainties in the \mathcal{P} values recovered from the tree-ring $\Delta^{14}\text{C}$ record.

O. Marchal
Department of Geology and Geophysics,
Woods Hole Oceanographic Institution,
Woods Hole, MA 02543, USA
E-mail: omarchal@whoi.edu
Tel.: +1-508-2893374
Fax: +1-508-4572187

Estimating these uncertainties is not trivial, as it requires accounting for the errors in the tree-ring $\Delta^{14}\text{C}$ data and in the model used to infer the \mathcal{P} variations from these data. A method that considers these two sources of error is necessary for a rigorous estimation of the \mathcal{P} changes implied by the tree-ring $\Delta^{14}\text{C}$ record.

In this paper, we attempt to demonstrate the power of a method of optimal estimation theory by using a tree-ring $\Delta^{14}\text{C}$ record with a simple box model of the global ^{14}C cycle to produce an estimate of the time evolution of ^{14}C production in the atmosphere over the Holocene. Optimal estimation methods—known variously as “state estimation” (e.g., in oceanography) or “data assimilation” (e.g., in meteorology)—were identified as a particular class of “inverse methods” (e.g., Wunsch 1996). In the broadest terms, they are directed at estimating in some optimal fashion the time evolution of the state of a physical system, given noisy data and an imperfect dynamical model of the system. In our problem, the system is the global ^{14}C cycle, the state includes, among other quantities, the production of ^{14}C in the atmosphere, and the data are the tree-ring $\Delta^{14}\text{C}$ data. If the time at which an estimate of the state is desired coincides with the last measurement point of the data span, the process of determining the estimate is called filtering (a popular filtering method is the Kalman filter). If this time is within the data span, it is called smoothing. In our problem, a smoothing procedure is obviously warranted, as we wish to estimate \mathcal{P} at a series of discrete times within the span of the tree-ring $\Delta^{14}\text{C}$ record. Albeit promising, applications of optimal estimation methods to geochemical problems are scarce. For example, their application to the interpretation of gaseous components from ice cores has been explored only very recently (Trudinger et al. 2002a, b).

The specific methodology used in this paper is the so-called Rauch-Tung-Striebel (RTS) smoother (Rauch et al. 1965). In essence, the method is a form of least-squares fit of a model to data, both suitably weighted to reflect their relative errors. The RTS smoother is used to extract information about the time evolution of the production of ^{14}C in the atmosphere for the period 9400 year BC to AD 1900 year from the tree-ring $\Delta^{14}\text{C}$ record. Unlike previous attempts to infer production changes from the tree-ring record (e.g., Stuiver and Braziunas 1989, 1993a, b; Stuiver et al. 1991; Bond et al. 2001), our analysis formally considers the errors both in the ^{14}C measurements and in the model. On the other hand, the errors are considered to be purely random, i.e., not systematic. Whereas the systematic errors are obviously a major issue in any problem of data-model combination, we believe that our analysis provides a more rigorous, statistically-based interpretation of the tree-ring $\Delta^{14}\text{C}$ record.

The paper is organized as follows. Section 2 describes the RTS method, the tree-ring $\Delta^{14}\text{C}$ record, and the model of the global ^{14}C cycle. The results of the combination, including diagnostics of the analysis, our best estimate of the time evolution of ^{14}C production, and

sensitivity tests, are reported in Sect. 3. We compare in Sect. 4 our best production estimates with independent constraints on cosmogenic nuclide production over the Holocene from a variety of archives. The comparisons give insight into the internal consistency between different indicators of cosmogenic nuclide production during a period of relative climate stability. A spectral analysis of our \mathcal{P} estimates is conducted, and the implications of our results for the hypothesis of a solar forcing mechanism on Holocene climate variability (e.g., Bond et al. 2001) are discussed. Conclusions follow in Sect. 5.

2 Method

2.1 Rauch-Tung-Striebel smoother

In this section, we provide a heuristic description of the method of optimal estimation theory, which is used to combine the tree-ring $\Delta^{14}\text{C}$ record and the model of the global ^{14}C cycle (details about the method are reported in Appendix 1). The theory uses vector-matrix notation. The following conventions are adopted: nonbolded letters represent scalars, lowercase boldface letters denote vectors, and uppercase boldface letters are matrices. In the theory, the state variables of the physical system under consideration are the n elements of a state vector \mathbf{x} and the measurements on the system are the m elements of a measurement vector \mathbf{z} . A subscript such as i or j added to both vectors, e.g., \mathbf{x}_i and \mathbf{z}_j , means the corresponding vectors at some discrete time t_i or t_j .

The theory of optimal estimation introduces two basic equations: the “observation equation” and the “transition equation”. The observation equation expresses the $m \times 1$ measurement vector \mathbf{z}_i as a function of the $n \times 1$ state vector \mathbf{x}_i and a $m \times 1$ measurement error vector \mathbf{v}_i :

$$\mathbf{z}_i = \mathbf{H}_i \mathbf{x}_i + \mathbf{v}_i, \quad (1)$$

where the $m \times n$ matrix \mathbf{H}_i is the observation matrix. The equation states that any measurement performed on the system can be expressed as the sum of (i) a linear combination of the state variables of the system and (ii) a noise. The elements of the matrix \mathbf{H}_i are the coefficients appearing in the combinations. They may vary with time, as implied by the addition of subscript i . In our problem, \mathbf{z}_i is the collection of observations (tree-ring $\Delta^{14}\text{C}$ data) at time t_i relative to the global ^{14}C cycle, \mathbf{x}_i is the set of variables that completely describe the cycle in terms of the model, and \mathbf{v}_i includes the errors in the tree-ring $\Delta^{14}\text{C}$ data. The transition equation expresses the state vector \mathbf{x} at time t_{i+1} as a function of the state vector \mathbf{x} and a $p \times 1$ forcing vector \mathbf{w} , both at some earlier time t_i :

$$\mathbf{x}_{i+1} = \Phi_i \mathbf{x}_i + \Gamma_i \mathbf{w}_i, \quad (2)$$

where Φ_i is the $n \times n$ transition matrix for the state and Γ_i is the $n \times p$ transition matrix for the forcing. Again, both matrices may contain elements that vary with time,

as implied by the addition of subscript i . In our problem, Eq. 2 is the compact form of a model of the global ^{14}C cycle, where $\Phi_i \mathbf{x}_i$ represents, e.g., the exchanges of ^{14}C between different geochemical reservoirs and $\Gamma_i \mathbf{w}_i$ represents ^{14}C inputs to the reservoirs that are independent of the state \mathbf{x}_i .

The problem is how to combine the information provided by the measurements (as embodied by Eq. 1) and the a priori knowledge about the dynamical behavior of the system (Eq. 2), to estimate the state of the system \mathbf{x}_i such that some performance measure is maximized. The RTS methodology, which is used here to solve this problem, has two essential components: (i) a filter (the Kalman filter), which provides a first estimate of the state \mathbf{x}_i using the measurements up to and including those at time t_i ; and (ii) a smoother (the RTS smoother), which improves the filter estimates of \mathbf{x}_i by considering all the available measurements, including those posterior to t_i . Importantly, the solution provides an estimate of the uncertainties in the state variables, as well as of the state variables themselves. Several algorithms can be employed for the RTS smoother, the specific algorithm used in this study being detailed in Appendix 1.

2.2 Tree-ring data

In this section, we cast a reconstruction of atmospheric ^{14}C concentration into the canonical form (Eq. 1). We consider the decadal averages of $\Delta^{14}\text{C}$ calculated by Stuiver et al. (1998) for the period between 9400 year BC (11350 year BP) and AD 1900 year (50 year BP). These averages are entirely based on ^{14}C measurements on dendrodated wood samples. They exhibit well-known features, such as a long-term decrease and many shorter-term variations (Fig. 1a). The errors in the decadal $\Delta^{14}\text{C}$ (Stuiver et al. 1998) never exceed 7‰ for the aforementioned period (Fig. 1b). The $\Delta^{14}\text{C}$ data must be converted into data of atmospheric ^{14}C concentration, which is a state variable of the model (Sect. 2.3). As the model neglects fractionation effects in the global ^{14}C cycle, the relationship between atmospheric $\Delta^{14}\text{C}$ ($\Delta^{14}\text{C}_{a,i}$ in ‰) and atmospheric ^{14}C concentration ($x_{a,i}$ in mol m^{-3}) in the model is simply:

$$\Delta^{14}\text{C}_{a,i} = \left(\frac{x_{a,i}/x_a^*}{r^*} - 1 \right) 10^3, \quad (3)$$

where $x_a^* = 1.184 \times 10^{-2} \text{ mol m}^{-3}$ is a reference concentration of CO_2 in the atmosphere and $r^* = 1.176 \times 10^{-12}$ is a reference $^{14}\text{C}/^{12}\text{C}$ ratio of atmospheric CO_2 . The following quantities are therefore defined in the observation Eq. 1:

$$\mathbf{z}_i = z_i = r^* x_a^* (10^{-3} \Delta^{14}\text{C}_{tr,i} + 1), \quad (4)$$

$$\mathbf{H}_i = [1, 0, 0, 0, 0, 0], \quad (5)$$

where $\Delta^{14}\text{C}_{tr,i}$ is the tree-ring datum for time t_i (Fig. 1a) and $r^* x_a^* = 1.392 \times 10^{-14} \text{ mol m}^{-3}$ is a reference

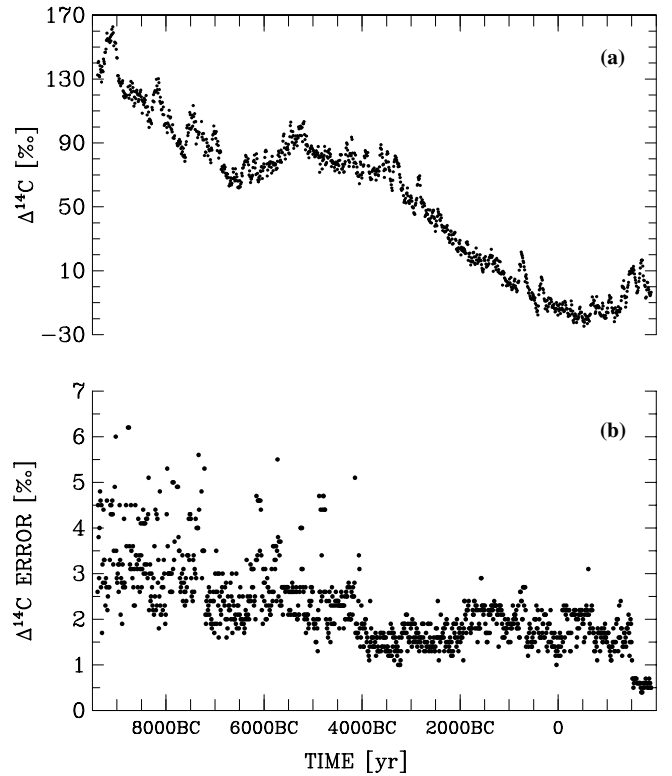


Fig. 1 Record of $\Delta^{14}\text{C}$ from ^{14}C measurements in wood samples dated dendrochronologically (a) and $\Delta^{14}\text{C}$ errors (b). The values in panels (a–b) are decadal averages (data from Stuiver et al. 1998)

concentration of ^{14}C in the atmosphere. If time t_i occurs within a decade for which no datum is available, the observation matrix vanishes, i.e., $\mathbf{H}_i = \mathbf{0}$.

The possibility of a sequential correlation in the measurement errors \mathbf{v}_i must be assessed, as the presence of such a correlation would violate an assumption (Eq. 11) which is used to derive the Kalman filter and RTS smoother (Appendix 1). The reported errors in the tree-ring $\Delta^{14}\text{C}$ data (Fig. 1b) show features that actually suggest the presence of sequential correlation. These features include a long-term trend in the error mean (the $\Delta^{14}\text{C}$ errors for the early Holocene are on average larger than the errors for the late Holocene) and many time intervals during which the error is virtually constant (reflecting most probably the rounding of the errors to the most significant figures). Bryson and Ho (1975) discussed two different approaches to account, in the RTS smoother, for the presence of sequential correlation in the measurement errors. Both approaches rely on the probability model $\mathbf{v}_{i+1} = \mathbf{v}_i + \Psi_i \mathbf{u}_i$, where Ψ_i controls the variance of the errors and \mathbf{u}_i has zero mean and is uncorrelated in time (i.e., $E(\mathbf{u}_i) = \mathbf{0}$ and $E(\mathbf{u}_i \mathbf{u}_j^T) = \mathbf{0}$ for $i \neq j$, where $E(\cdot)$ is the mean and T denotes the transpose). However, this model would not be a generally valid description of the errors in the tree-ring $\Delta^{14}\text{C}$ data, as it cannot accommodate the large number of time intervals during which the error is constant (Fig. 1b). Indeed, this would require (in addition to $\Psi_i = \mathbf{1}$,

perhaps a sensible choice) that the stochastic component of the error, \mathbf{u}_i , is constant during the intervals, i.e., $E(\mathbf{u}_i \mathbf{u}_j^T) \neq \mathbf{0}$ for $i \neq j$, which would violate the assumption in both approaches. Here we adopt the simplest approach, which is to assume that the data errors *are* sequentially uncorrelated, admitting that this is not an accurate description of some of the features in the error record. We will show that the diagnostics of the analysis do not question the validity of the results obtained with this assumption (Sect. 3.1).

2.3 Geochemical model

In this section, we formulate a box model of the global ^{14}C cycle in the canonical form (Eq. 2), which

$$\begin{bmatrix} -\left(\frac{Agf}{V_a} + \frac{1}{\tau_a} + \lambda\right) & \frac{1}{\tau_a} & 0 & \frac{\alpha Ag}{V_a} & \frac{(1-\alpha)Ag}{V_a} \\ \frac{1}{\tau_b} & -\left(\frac{1}{\tau_b} + \lambda\right) & 0 & 0 & 0 \\ 0 & 0 & -\left(\frac{J+J_{hd}}{V_d} + \lambda\right) & \frac{J+J_{hd}}{V_d} & 0 \\ \frac{\alpha Agf}{V_h} & 0 & \frac{J_{hd}}{V_h} & -\left(\frac{J+J_{hd}+\alpha Ag}{V_h} + \lambda\right) & \frac{J}{V_h} \\ \frac{(1-\alpha)Agf}{V_l} & 0 & \frac{J}{V_l} & 0 & -\left(\frac{J+(1-\alpha)Ag}{V_l} + \lambda\right) \end{bmatrix}$$

is required for the application of the RTS smoother. There is obviously arbitrariness in the choice of the model, and the results of the analysis should be sensitive to this choice to a certain extent. On the other hand, we will explore the sensitivity of these results to the (supposedly purely random) errors in the model (Sect. 3.3). It is hoped that this will give insight into their robustness. We consider a model with five reservoirs: the atmosphere (labeled “a”), the land biosphere (“b”), the high-latitude surface ocean (“h”), the low-latitude surface ocean (“l”), and the deep ocean (“d”; Fig. 2). Radiocarbon is produced in the atmosphere, exchanged with the land biosphere to represent the photosynthetic uptake and respiratory release of $^{14}\text{CO}_2$, and exchanged with the surface oceans to represent the air-sea fluxes of $^{14}\text{CO}_2$. In the ocean, radiocarbon is transported by a meridional overturning circulation (solid arrows in Fig. 2) and a bidirectional mixing between the high-latitude surface ocean and the deep ocean (dashed arrow in Fig. 2). Several studies used a similar, three-box representation of the world oceans to simulate the carbon cycle on the time scale of several millennia (e.g., Sarmiento and Toggweiler 1984; Siegenthaler and Wenk 1984; Toggweiler 1999; Legrand and Alverson 2001). For simplicity, the bidirectional mixing between the deep and low latitude surface oceans and between the high and low latitude surface oceans is omitted, as in previous studies (e.g., Sarmiento and Toggweiler 1984; Toggweiler 1999). Nevertheless, the impact of these terms on our results will be tested (Sect. 3.3).

Now, consider the model formulation. The state variables of the model are the concentration of ^{14}C in each reservoir (in units of mol m^{-3}). The state vector is thus $\mathbf{x}^T = [x_a, x_b, x_d, x_h, x_l]$ (a dot subscript is added to distinguish \mathbf{x} from the vector \mathbf{x} that is of higher dimension and effectively used in Eqs. 1, 2; see below and Appendix 2). The time evolution of each state variable is governed by an ordinary differential equation. These equations can be expressed with the compact notation:

$$\frac{d\mathbf{x}}{dt} = \mathbf{F}\mathbf{x} + \mathbf{G}\mathbf{w}, \quad (6)$$

where \mathbf{F} is the transition matrix for the state \mathbf{x} and \mathbf{G} is the transition matrix for the forcing \mathbf{w} . The matrix \mathbf{F} is: The definition and value of each quantity in this matrix

is reported in Table 1. The transition matrix \mathbf{G} is a 5×1 vector as \mathbf{w} includes only one element, i.e., the production of ^{14}C in the atmosphere (\mathcal{P}). Thus $\mathbf{G}^T = [1, 0, 0, 0, 0]$ and $\mathbf{w} = w = \mathcal{P}$.

Insight into the dynamical model (6), its response to \mathcal{P} changes in particular, is obtained from the eigenvalues of \mathbf{F} , which we note as λ_j , where $j=1,2,\dots,5$ (e.g., Luenberger 1979). For a constant \mathbf{F} the ^{14}C concentration in each reservoir can be expressed as a linear combination of five terms, where the j th term includes the pure exponential $\exp(\lambda_j t)$ (Lasaga 1980). The intrinsic time scales of model (6) amount to 2.9, 4.5, 12.2, 134.1, and 8267.0 yr (Table 2). The rate of attainment of steady state for the geochemical cycle as a whole is given by the negative eigenvalue, λ_1 , with the smallest absolute value, as this is the last term to decay in the combinations. For model (6) the intrinsic time scale $|\lambda_1|^{-1}$, interpreted as the “collective geochemical cycle response time” (Lasaga 1980), is equal, within the uncertainty of our numerical calculations, to the mean decay period of ^{14}C , i.e., $|\lambda_1| = \lambda$, where λ is the decay constant of ^{14}C (Table 1).

The ordinary differential equations (6) are approximated by finite difference equations using the first order Euler scheme. The difference equations are denoted by the compact form:

$$\mathbf{x}_{i+1} = \Phi_i \mathbf{x}_i + \Gamma_i \mathbf{w}_i, \quad (7)$$

where Φ_i is the transition matrix for \mathbf{x}_i and Γ_i is the transition matrix for \mathbf{w}_i . We assume that all quantities in Φ_i are constant in time except the piston velocity g_i

Fig. 2 Schematic diagram of the five-reservoir model of the global ^{14}C cycle used in this study. The *staggered arrow* represents the production of ^{14}C in the atmosphere. The *dashed arrows* denote the photosynthetic uptake by, and the respiratory release from the land biosphere, the air-sea gas exchanges, and the bidirectional mixing between oceanic reservoirs. The *solid arrows* depict a meridional overturning circulation

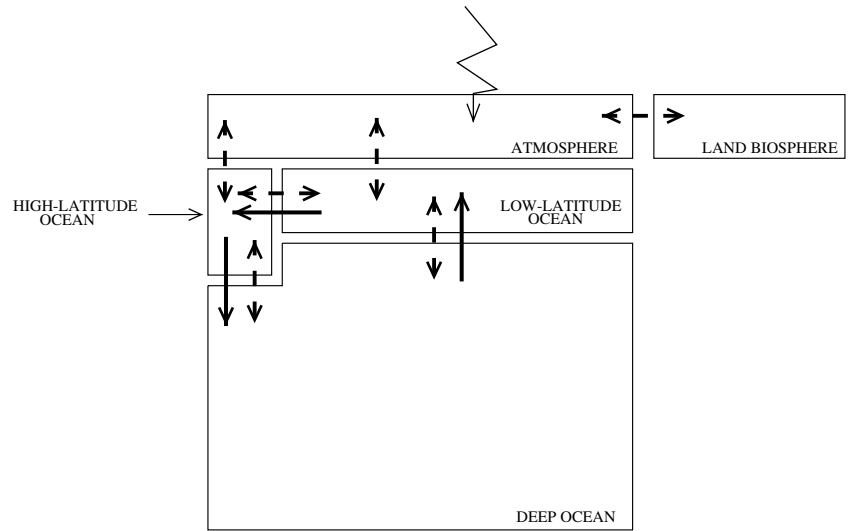


Table 1 Parameters of the global ^{14}C cycle model

r_e	Radius of earth	6,371 km	
h_a	Scale height of atmosphere	8,320 m	Stocker and Wright (1996)
h_l	Depth of low-latitude surface ocean	100 m	Toggweiler and Sarmiento (1985)
h_h	Depth of high-latitude surface ocean	250 m	Toggweiler and Sarmiento (1985)
V	Volume of ocean	$1.292 \times 10^{18} \text{ m}^3$	Levitus (1982)
S	Area of ocean	$3.49 \times 10^{14} \text{ m}^2$	Sverdrup et al. (1942)
α	Fractional area of high-latitude surface ocean	0.15	Toggweiler and Sarmiento (1985)
V_a	Volume of atmosphere	$4.244 \times 10^{18} \text{ m}^3$	$4\pi r_e^2 h_a$
V_l	Volume of low-latitude surface ocean	$2.966 \times 10^{16} \text{ m}^3$	$(1-\alpha)Sh_l$
V_h	Volume of high latitude surface ocean	$1.309 \times 10^{16} \text{ m}^3$	αSh_h
V_d	Volume of deep ocean	$1.249 \times 10^{18} \text{ m}^3$	$V - V_l - V_h$
DIC*	Reference content of dissolved inorganic C in ocean	2.250 mol m^{-3}	
x_a^*	Reference content of CO_2 in atmosphere	$1.184 \times 10^{-2} \text{ mol m}^{-3}$	
f	Factor to convert x_a in units of oceanic content	190	DIC*/ x_a^*
I_a	C inventory in reference atmosphere	730 PgC	IPCC (2001)
I_b	C inventory in reference land biosphere	2,000 PgC	IPCC (2001)
F	C flux between atmosphere and land biosphere	120 PgC yr^{-1}	IPCC (2001)
τ_a	Residence time of C in atmosphere w.r.t. F	6.08 yr	I_a/F
τ_b	Residence time of C in land biosphere w.r.t. F	16.7 yr	I_b/F
J	Meridional overturning circulation	20 Sv	Toggweiler and Sarmiento (1985)
J_{hd}	Mixing between high-latitude surface ocean and deep ocean	60 Sv	Toggweiler and Sarmiento (1985)
J_{dl}	Mixing between deep and low-latitude surface oceans	1 Sv	Toggweiler and Sarmiento (1985)
J_{hl}	Mixing between high and low-latitude surface oceans	10 Sv	Toggweiler and Sarmiento (1985)
g^*	Reference piston velocity for air-sea gas exchange	7.13 m yr^{-1}	Stocker and Wright (1996)
r^*	Reference $^{14}\text{C}/^{12}\text{C}$ ratio of atmospheric CO_2	1.176×10^{-12}	
λ	Decay constant of ^{14}C	$8,267^{-1} \text{ yr}^{-1}$	

Table 2 Eigenvalues of \mathbf{F} and intrinsic time scales of the continuous system $d\mathbf{x}/dt = \mathbf{F}\mathbf{x} + \mathbf{G}\mathbf{w}$

j	Eigenvalue λ_j (yr^{-1})	Intrinsic time scale $ \lambda_j ^{-1}$ (yr)
1	-0.000121	8267.0
2	-0.007458	134.1
3	-0.081801	12.2
4	-0.222457	4.5
5	-0.340450	2.9

for the air-sea gas exchange. The consideration of a variable g_i allows us to represent in the model the effects on atmospheric $\Delta^{14}\text{C}$ of the changes in atmospheric CO_2

concentration (x_a^c below) during the Holocene. The following relation is used (Stocker and Wright 1996):

$$g_i = g^* \frac{x_{a,i}^c}{x_{a,0}^c}, \quad (8)$$

where g^* is a reference velocity (Table 1), $x_{a,i}^c$ is the concentration at time t_i , and $x_{a,0}^c$ is the concentration at the initial time of the analysis (9400 year BC). To constrain the changes in atmospheric CO_2 concentration we use the CO_2 record from the Dome C ice core (Fig. 3; Flückiger 2002). In order to obtain a CO_2 value for each discrete time t_i of the analysis, the raw CO_2 data for Dome C are interpolated onto a regular temporal grid

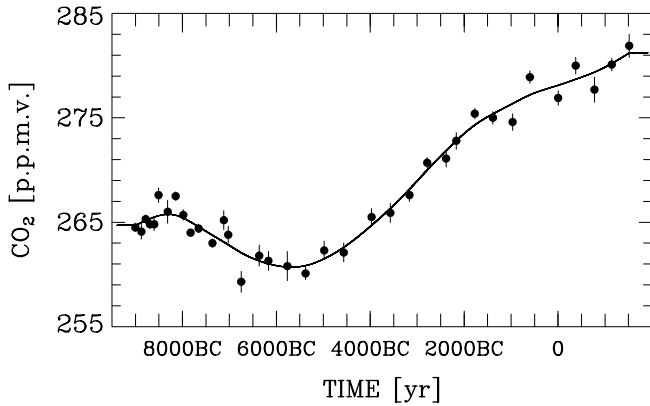


Fig. 3 Records of CO_2 concentration from the Dome C ice core (data from Flückiger 2002). The *dots* are the mean values on several samples and the *vertical bars* are their standard errors. The *solid curve* is the cubic smoothing spline calculated with a smoothing parameter equal to 10

using a cubic smoothing spline with a smoothing parameter equal to 10 (Fig. 3). Note that the choice of the CO_2 record does not affect our major results, as the effects of changing atmospheric CO_2 on the inferred ^{14}C production variations are actually very small (Sect. 3.3).

As for the measurement errors \mathbf{v}_i , we must assess whether the forcing \mathbf{w}_i is correlated in time. Indeed, the presence of a sequential correlation in the forcing would violate an assumption (Eq. 12) which is used to derive the Kalman filter and RTS smoother (Appendix 1). Time correlation in the forcing $\mathbf{w}_i = \mathcal{P}_i$ is actually expected on geophysical grounds. A substantial fraction of the variability in the production of cosmogenic nuclides presumably stems from the variability in the geomagnetic field and solar activity. Although both phenomena may conceivably contain a random component, they vary relatively slowly in time and certainly are not white sequences in the present application. That is, if we were to use a relatively small time step in (7) (we use $\Delta t = 1$ year), we would find that the resulting forcing \mathbf{w}_i would be strongly correlated in time. The presence of colored system forcing is not a fundamental problem, however, as different approaches are known for dealing with it. The specific approach used in this study is detailed in Appendix 2.

3 Results

3.1 Diagnostics

The combination of the tree-ring $\Delta^{14}\text{C}$ data with the global ^{14}C cycle model requires the specification of different quantities (Appendix 1): (1) the covariance matrix for the measurement errors \mathbf{R}_i , (2) an estimate of the initial state $\hat{\mathbf{x}}_0$, (3) the covariance matrix for the errors in this state $\hat{\mathbf{P}}_0$, and (4) the covariance matrix for the model errors \mathbf{Q} . The determination of each of these quantities is detailed in Appendix 3. Consider a

particular solution to the combination problem obtained with $V_a/\Delta t\sqrt{q\mathcal{P}} = 3 \text{ mol yr}^{-1}$, where V_a is the volume of the model atmosphere (Table 1) and $q\mathcal{P}$, an element of \mathbf{Q} , governs the amount by which \mathcal{P} can change from one discrete time to the next in the model (Appendix 2). A visual comparison between the tree-ring $\Delta^{14}\text{C}$ data, the Kalman filter estimates of atmospheric $\Delta^{14}\text{C}$, and the RTS smoother estimates of atmospheric $\Delta^{14}\text{C}$ during three portions of the Holocene, shows how the methods of optimal estimation operate (Fig. 4a–c). In particular, it reveals how the filter and the smoother negotiate different features in the tree-ring record, such as high frequency variability (e.g., between 7900–8000 year BC; Fig. 4a), missing data (at ~ 7800 year BC; Fig. 4a), and varying data error (Fig. 4a–c). Although a visual comparison is instructive, it does not provide an objective assessment of the quality of the analysis. To obtain such an assessment, we consult two particular diagnostics of the analysis. The first diagnostic is based on the vector difference between the measurement \mathbf{z}_i and the estimate

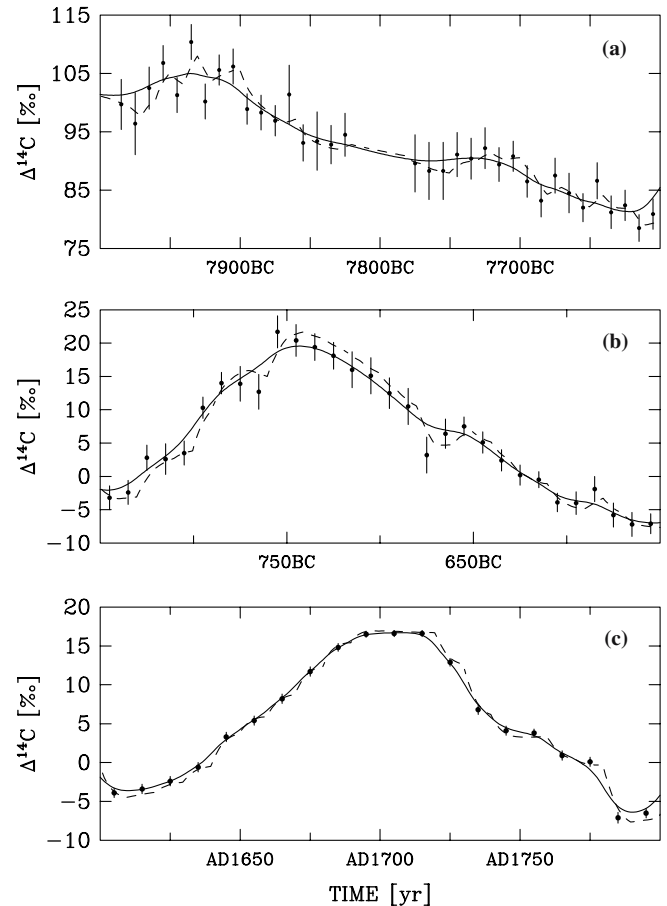


Fig. 4 Three portions (a–c) of the tree-ring $\Delta^{14}\text{C}$ record (*dots*), of the time series of the Kalman filter estimate of atmospheric $\Delta^{14}\text{C}$ (*dashed line*), and of the time series of the RTS smoother estimate of atmospheric $\Delta^{14}\text{C}$ (*solid line*). The errors in the tree-ring $\Delta^{14}\text{C}$ data (*vertical lines*) are also shown. The optimal estimates were obtained with $V_a/\Delta t\sqrt{q\mathcal{P}} = 3 \text{ mol yr}^{-1}$. Panel (c) corresponds chronologically to the Maunder minimum of solar activity

of the state before measurement $\bar{\mathbf{x}}_i$ (Appendix 1), $v_i = \mathbf{z}_i - \mathbf{H}_i \bar{\mathbf{x}}_i$, referred to as the ‘‘innovation’’. Mehra (1970) showed that for an optimal filter the innovation sequence v_i is a normal (gaussian) white sequence under some conditions. One of the conditions is that both the system and the filter have reached steady-state. Although strictly steady state cannot occur for our problem (e.g., Φ_i and \mathbf{R}_i are not constant in time), it is instructive to consult the (probability) density function of the innovation v_i normalized to the square root of its variance $\mathbf{H}_i \bar{\mathbf{P}}_i \mathbf{H}_i^T + \mathbf{R}_i$ ($\bar{\mathbf{P}}_i$ being the covariance matrix for the errors in \mathbf{x}_i ; Appendix 1). In our case, the normalized innovation is the scalar v_i^* defined as

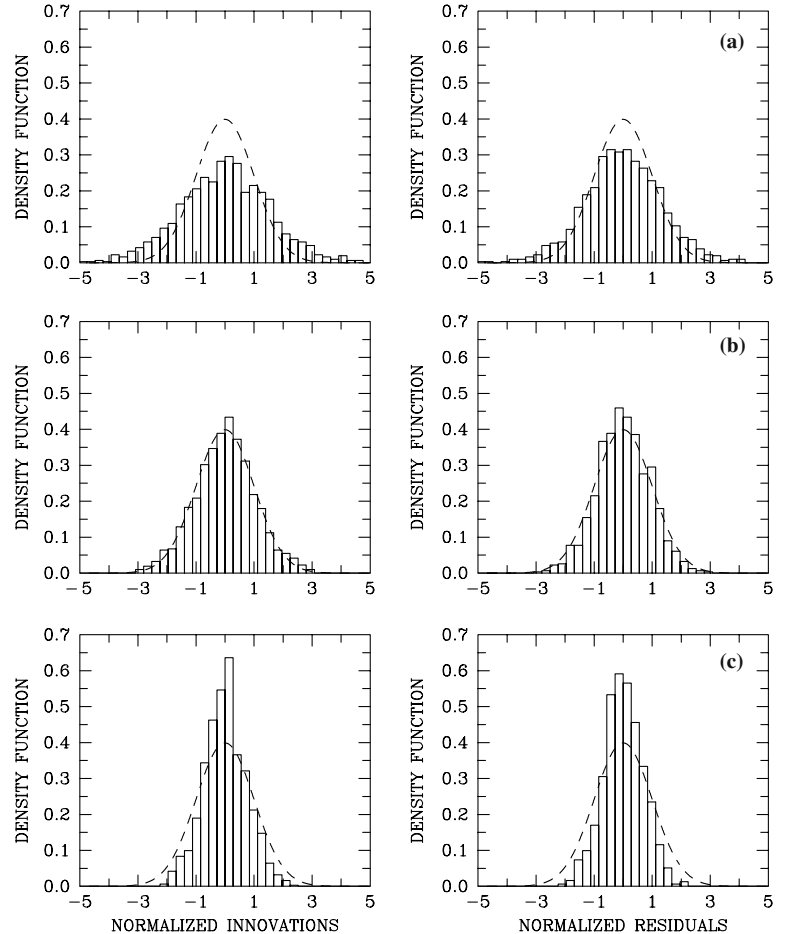
$$v_i^* = \frac{z_i - \bar{x}_{a,i}}{\sqrt{\bar{p}_{a,i} + r_i}}, \quad (9)$$

where $\bar{p}_{a,i} = E(x_{a,i} - \bar{x}_{a,i})^2$ is the element in the first row and first column of $\bar{\mathbf{P}}_i$, and r_i is the data error squared (Appendix 3). The second diagnostic is based on the vector difference between the measurement \mathbf{z}_i and the RTS smoother estimate of the state $\tilde{\mathbf{x}}_i$ (Appendix 1), $\mu_i = \mathbf{z}_i - \mathbf{H}_i \tilde{\mathbf{x}}_i$, which we call the smoother residual. We will consult the density function of the smoother residual μ_i normalized to the square root of the variance of the data errors \mathbf{R}_i . In our case, the normalized smoother residual is the scalar μ_i^* defined as

$$\mu_i^* = \frac{z_i - \tilde{x}_{a,i}}{\sqrt{r_i}}. \quad (10)$$

To illustrate the benefits of v_i^* and μ_i^* as diagnostics, we consider their density functions for three different analyses with $V_a/\Delta t\sqrt{q_p} = 1, 3,$ and 6 mol yr^{-1} (Fig. 5a–c). The analysis with $V_a/\Delta t\sqrt{q_p} = 1 \text{ mol yr}^{-1}$ permits only a relatively small variation of ^{14}C production from one discrete time to the next in the model, which implies a relatively small capability of the model to fit the tree-ring $\Delta^{14}\text{C}$ data. Accordingly, the distributions of v_i^* and μ_i^* are too flat compared to the normal distribution (Fig. 5a). An unreasonable fraction of the smoother estimates $\tilde{x}_{a,i}$ are removed by more than $2\sqrt{r_i} = 2\sigma_i$ from the tree-ring data. The analysis with $V_a/\Delta t\sqrt{q_p} = 6 \text{ mol yr}^{-1}$ permits much higher variation of ^{14}C production and capability to fit the data. Here the distributions of v_i^* and μ_i^* are too peaked compared to the normal (Fig. 5c). That is, the fit of $\tilde{x}_{a,i}$ to the data is not warranted given the errors in these data. The analysis with $V_a/\Delta t\sqrt{q_p} = 3 \text{ mol yr}^{-1}$ results in distributions of v_i^* and μ_i^* that are much more consistent with the normal distribution (Fig. 5b). Although additional analyses could be conducted and a more detailed examination of diagnostics is possible (e.g., the best adjustments to the normal distribution could be sought, formal tests of

Fig. 5 Diagnostics of the Kalman filter and RTS smoother. The *left panels* show (probability) density functions of the innovations normalized to their standard deviations. The *right panels* show density functions of the smoother residuals normalized to the observation errors (uncertainties in the tree-ring $\Delta^{14}\text{C}$). The density functions correspond to the case where $V_a/\Delta t\sqrt{q_p} = 1 \text{ mol yr}^{-1}$ (a), 3 mol yr^{-1} (b), and 6 mol yr^{-1} (c). The *dashed curve* in each panel represents the standardized normal density function



normality and randomness could be performed, etc.), we consider in the sequel the analysis with $V_a/\Delta t\sqrt{q_P} = 3 \text{ mol yr}^{-1}$ as providing our best estimate of the time evolution of ^{14}C production over the Holocene. This estimate is described in some detail in Sect. 3.2 and its robustness is assessed in Sect. 3.3.

3.2 Optimal estimate of ^{14}C production changes

Our best estimate of the time evolution of \mathcal{P} has a rich structure, characterized by apparent changes in mean level and some high frequency variability, which have a comparable order of magnitude of $\mathcal{O}(10^2)$ mol yr^{-1} (Fig. 6a). Whereas the mean level shows apparent changes, the production variations do not exhibit a conspicuous long-term decline such as in the concentration ($\Delta^{14}\text{C}$) record from which these variations are inferred (Fig. 1a). This suggests that the decline in the tree-ring $\Delta^{14}\text{C}$ data reflects a slow adjustment of the concentration to production changes, a possibility which could have been anticipated from the long collective response time of the global ^{14}C cycle (Sect. 2.3). Our best estimate of the time evolution of \mathcal{P} seems to show similarities with previous estimates also based on the tree-ring record but obtained from procedures that are not statistically

grounded (e.g., Fig. 19 of Stuiver et al. 1991; Fig. 7 of Stuiver and Braziunas 1993b).

In contrast to previous studies, our analysis provides an estimate of the error in the ^{14}C production rates recovered from the tree-ring record (Fig. 6b). Overall, the relative error never exceeds 8% and is generally much lower. The changes in mean level and the high frequency variability in \mathcal{P} mentioned above are thus significant features, a statement that must be tempered by the fact that our analysis does not consider systematic errors. The time evolution of the \mathcal{P} error can be explained as follows (Fig. 6b). The rapid error increase at the very beginning of the time series indicates that our a priori estimate of the errors in the initial state ($\hat{\mathbf{P}}_0$; Appendix 3) was too optimistic, which is rapidly accounted for in the analysis. The \mathcal{P} error exhibits a subsequent decrease, which, albeit relatively slow, is faster than the collective response time = 8267 yr. The error decrease is due to the increasing availability of $\Delta^{14}\text{C}$ data to estimate ^{14}C production. The small errors $<5 \text{ mol yr}^{-1}$ at the end of the period reflects the small uncertainties $<1\%$ of the tree-ring $\Delta^{14}\text{C}$ data for that time (Fig. 1b). Finally, the rapid error increase at the end of the period is due to the fact that the production estimate is not constrained by $\Delta^{14}\text{C}$ values posterior to AD 1900 year, i.e., the filter and smoother estimates of \mathcal{P} are similar for the last measurement point (Eq. 19; Appendix 1).

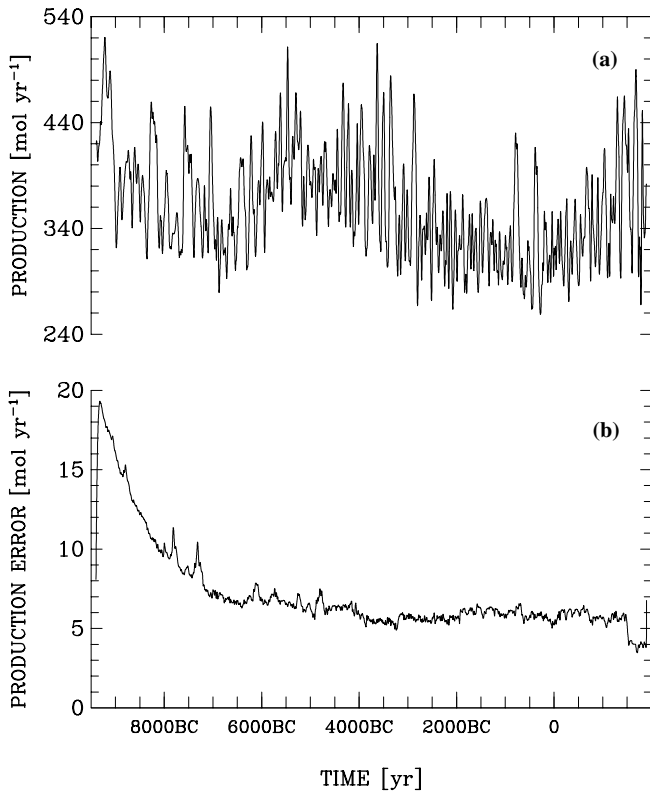


Fig. 6 **a** Optimal estimate of the time evolution of ^{14}C production in the atmosphere. **b** Error in this estimate

3.3 Sensitivity tests

In this section, we assess the robustness of our best estimate of the time evolution of \mathcal{P} described in the previous section. Different analyses are conducted, each with a different value of a particular quantity introduced in the estimation process (Appendix 3). The resulting estimates of \mathcal{P} are compared to our best estimates of \mathcal{P} on the basis of the cross-correlation coefficient at zero lag and the mean of the absolute differences between the two \mathcal{P} estimates (Table 3). Consider first the sensitivity of our results to the covariance of the model errors \mathbf{Q} . The sensitivity to the variances $q_k = E(w_k - \bar{w}_k)^2$, where $k \in \{a, b, d, h, l\}$, is tested by introducing the fraction ϵ , where $q_k = (\epsilon \hat{x}_{k,0})^2$, ϵ being taken the same for the stochastic component for each state variable (for our best estimates of \mathcal{P} we used $\epsilon = 0$; Appendix 3). The above formulation implies that the error in the model equations could lead, in one time step (1 yr), to a concentration change equal to $\sim \epsilon$ times the initial concentration in the reservoir. Were the error always be systematic and the exchanges between the reservoirs to vanish, it would produce in each reservoir a hypothetical cumulative change over the investigation period equal to $\sim 11,300\epsilon$ times the initial concentration. Assuming $\epsilon = 10^{-4}$ (hypothetical cumulative change $\sim 100\%$ the initial concentration) leads to a cross-correlation coefficient = 1.00 and a mean difference of only 2 mol yr^{-1} . Using $\epsilon = 10^{-3}$ results in

Table 3 Sensitivity of the optimal estimates of ^{14}C production

Analysis		Cross-correlation ^a	Mean difference ^b (mol yr ⁻¹)
ϵ	10^{-4}	1.00	2
ϵ	10^{-3}	0.84	24
θ	10	1.00	2
h_a	5,550 m	0.99	10
h_a	11090 m	1.00	10
h_l	67 m	1.00	2
h_l	133 m	1.00	1
h_h	167 m	1.00	0
h_h	333 m	1.00	0
α	0.10	1.00	5
α	0.20	1.00	4
g_i	7.13 m yr ⁻¹	1.00	2
g^*	4 m yr ⁻¹	1.00	14
g_i	10 m yr ⁻¹	1.00	7
J	10 Sv	0.99	16
J	30 Sv	1.00	9
J_{hd}	3 Sv	0.99	15
J_{hd}	300 Sv	1.00	5
J_{dl}	1 Sv	1.00	1
J_{hl}	10 Sv	1.00	5
τ_a	3 yr	0.98	21
τ_a	9 yr	1.00	7
τ_b	10 yr	0.99	9
τ_b	24 yr	1.00	9

^a Cross-correlation coefficient at zero lag between the time evolution of \mathcal{P} in the particular analysis and the time evolution of \mathcal{P} in the reference analysis. ^b Mean of the absolute differences between \mathcal{P} in the particular analysis and \mathcal{P} in the reference analysis.

a cross-correlation coefficient of 0.84 and a mean difference of 24 mol yr⁻¹. With $\epsilon = 10^{-3}$, however, the density function of the normalized innovations and normalized smoother residuals is much too peaked compared to the normal distribution (not shown). Thus, the \mathcal{P} estimates inferred from the tree-ring record appear relatively insensitive to the diagonal elements of \mathbf{Q} for reasonable choices of ϵ . Consider then the sensitivity to the covariance of the errors in the initial state $\hat{\mathbf{P}}_0$. The sensitivity to the error variances $\hat{p}_{k,0}$, where $k \in \{b, d, h, l, \mathcal{P}\}$, is tested by introducing the fraction θ , where $\hat{p}_{k,0} = \hat{p}_{a,0}(\theta \hat{x}_{k,0} / \hat{x}_{a,0})^2$ (for our best estimates of \mathcal{P} we used $\theta = 1$). Assuming $\theta = 10$ leads to a cross-correlation = 1.00 and a mean difference = 2 mol yr⁻¹. All the other analyses, which are based on a different value of a model parameter, result in a cross-correlation coefficient that is similarly very high, whereas the mean difference varies between the analyses (Table 3). For example, consideration of the bidirectional mixing between the deep and low-latitude surface oceans (J_{dl}) and between the high and low-latitude surface oceans (J_{hl}) has a negligible influence. Using a 3-box ocean model similar to ours, Toggweiler and Sarmiento (1985) adopted $J_{dl} = 1$ Sv (1 Sv = 10^6 m³ s⁻¹) and $J_{hl} = 10$ Sv to fit chemical observations for the preindustrial ocean and atmosphere. Assuming $J_{dl} = 1$ Sv ($J_{hl} = 10$ Sv) leads to a cross-correlation of 1.00 (1.00) and a mean difference of 1 (5) mol yr⁻¹. In summary, the changes in our best \mathcal{P} estimates appear robust.

4 Discussion

4.1 Comparison with independent evidence

In this section, we compare our best estimate of the time evolution of \mathcal{P} with independent evidence of changes in the production of cosmogenic nuclides in the atmosphere between 9400 year BC and AD 1900 year. First, we consider a relatively recent compilation of magnetic measurements on archeological samples (Yang et al. 2000). The archeointensity data set (3243 values) is based on samples from the European region (2203) and the rest of the world (1040). It is almost three times larger than the one of McElhinny and Senanayake (1982) and does not show “major differences” with respect to this earlier compilation (Yang et al. 2000). The data set suggests long-term changes in the VADM (Fig. 7b) that visually resemble the changes in \mathcal{P} (Fig. 7a). For a more objective comparison, we average the \mathcal{P} values in each time interval for which an estimate of VADM is available (Yang et al. 2000), and plot the average \mathcal{P} versus these estimates (Fig. 8a). Although models suggest a power-law dependence of \mathcal{P} on the intensity of the geomagnetic field (for a review see Frank 2000), the data do not support or refute a particular dependence given their relatively small number and high dispersion (Fig. 8a). For example, the pattern in the linear regression residuals does not seem inconsistent with a linear relationship between \mathcal{P} and VADM (Fig. 8b; note that no attempt is made in the regression analysis to consider the errors in both variables). The linear correlation coefficient between both variables amounts to -0.76 with a significance level $p < 0.01$ ($n = 14$). Thus, approximately $0.76^2 = 58\%$ of the variance of \mathcal{P} is accounted for by linear regression on VADM data. A (negative) linear relationship between both variables would be highly significant assuming that their underlying joint distribution is binormal (Brownlee 1965). We consider the rank correlation coefficient Kendall tau as another measure of the intensity of the relation between the two random variables (Kendall and Gibbons (1990); p 41, Eq. 3.3). This coefficient is based on the ranking (not directly on the values) of the variables and measures the intensity of a monotonic relationship between them. Using this other measure of correlation is motivated by the fact that testing the significance of rank correlation requires weaker assumptions about the distribution of the variables than linear correlation (e.g., binormality is not required). The rank correlation coefficient amounts to -0.67 with a p value < 0.01 (using Table 1 of Appendix in Kendall and Gibbons (1990)). That is, \mathcal{P} and VADM show a negative monotonic relation, which also is highly significant.

Second, we compare our best estimates of ^{14}C production with a recent record of relative paleointensity (RPI) obtained from magnetic measurements on sediment core MD99-2220 raised from the St. Lawrence Estuary (St. Onge et al. 2003). Owing to the high

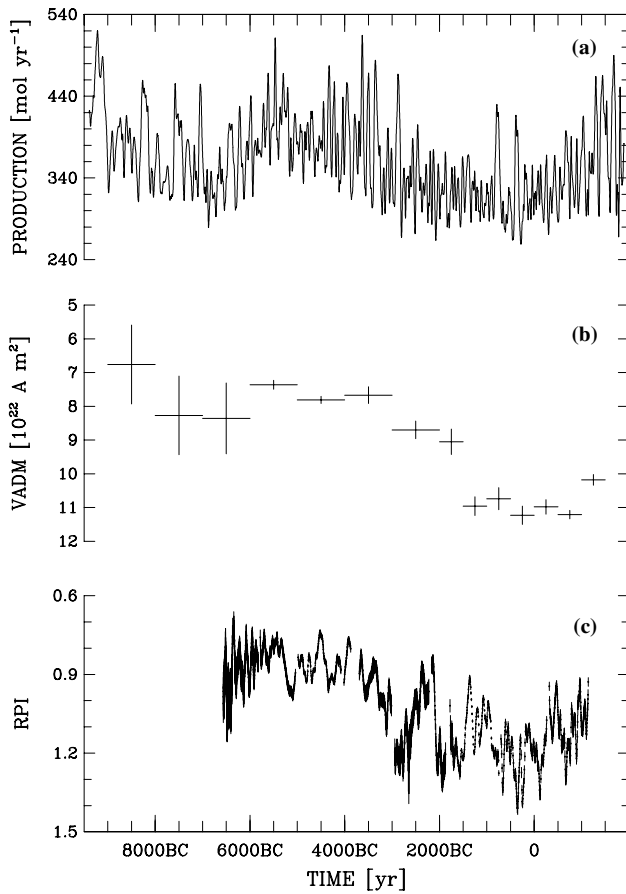


Fig. 7 **a** Optimal estimate of the time evolution of ^{14}C production in the atmosphere. **b** Record of the virtual axial dipole moment based on a compilation of magnetic measurements on archeological samples. The *horizontal bars* denote the time intervals for which an average value of VADM has been estimated and the *vertical bars* denote the 95% confidence intervals for the averages (data from Yang et al. 2000). **c** Record of relative paleointensity based on magnetic measurements on sediment core MD99-2220 raised from St. Lawrence Estuary (eastern Canada). The *vertical bars* are one standard deviation about the mean (data from St. Onge et al. 2003)

accumulation rates, these data have a much higher temporal resolution than the archeomagnetic data (Fig. 7). The scatter plot of our \mathcal{P} estimates versus RPI data for MD99-2220 suggests a nonlinear pattern, with relatively high \mathcal{P} values at low and high paleointensities (Fig. 9a). The linear regression residuals suggest a systematic, *u*-shaped pattern (Fig. 9b). Thus, a linear model does not appear not to be a valid description of the relation between our \mathcal{P} estimates and the paleointensities in MD99-2220. The rank correlation coefficient between both variables amounts to -0.33 ($n=1207$; $p < 0.01$). Although the Kendall tau is statistically more robust than the linear correlation coefficient, the pattern in the scatter plot suggests that the rank correlation statistics should be interpreted with caution as well.

Third, we compare our best estimates of \mathcal{P} with ^{10}Be concentration data from the GISP2 ice core, Central Greenland (Finkel and Nishiizumi 1997). For the

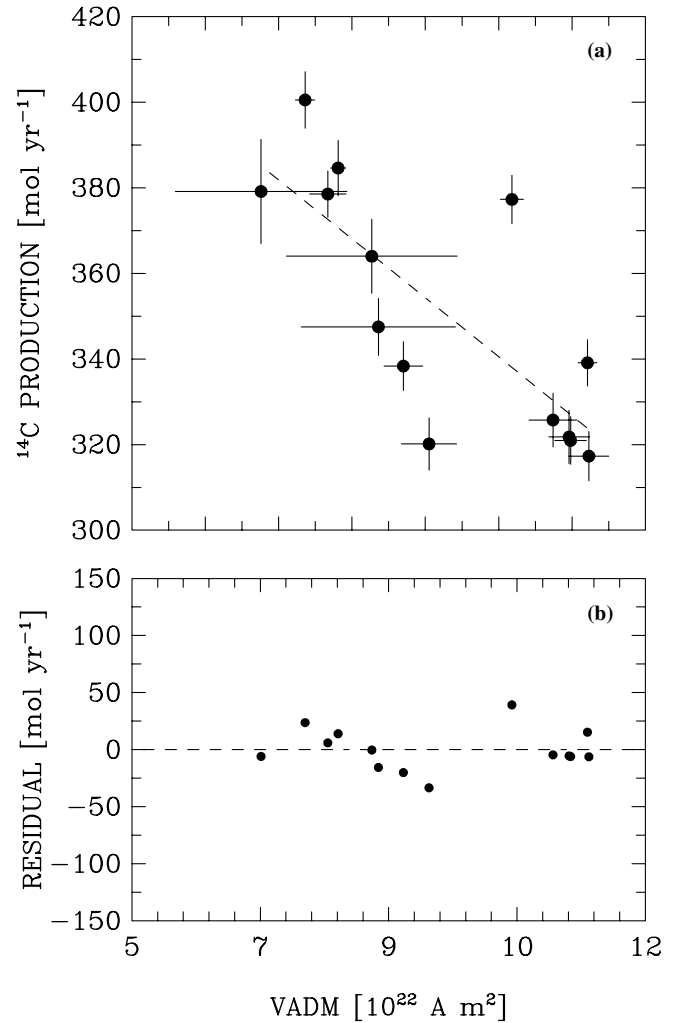


Fig. 8 **a** Scatter plot of the optimal estimates of ^{14}C production (\mathcal{P}) versus VADM estimates from archeomagnetic data. The \mathcal{P} values are the averages in the time intervals for which an estimate of VADM is available. The errors in ^{14}C production estimates (*vertical bars*) are the errors at the middle of these intervals. The errors in VADM (*horizontal bars*) are the 95% confidence intervals. The *dashed line* is the linear regression line. **b** Linear regression residuals (difference between \mathcal{P} and its value on the regression line) versus VADM estimates. The *dashed line* is the zero line (VADM data from Yang et al. 2000)

comparison, we follow Finkel and Nishiizumi (1997) by using the GISP2 chronology of Meese et al. (1994) to assign absolute ages to the depth intervals for which ^{10}Be concentration has been measured (Fig. 10b). Our \mathcal{P} estimates are averaged in these intervals for a consistent comparison, and the scatter plot is produced (Fig. 11a). Previous studies assumed that ^{10}Be concentration in Greenland ice of Holocene age is directly proportional to the global production rate of ^{10}Be as to that of ^{14}C (e.g., Beer et al. 1988; Yiou et al. 1997). The linear regression residuals do not show a clear pattern that would contradict a linear relation between \mathcal{P} and ^{10}Be concentration in GISP2 (Fig. 11b). The linear correlation coefficient between both variables amounts to 0.48

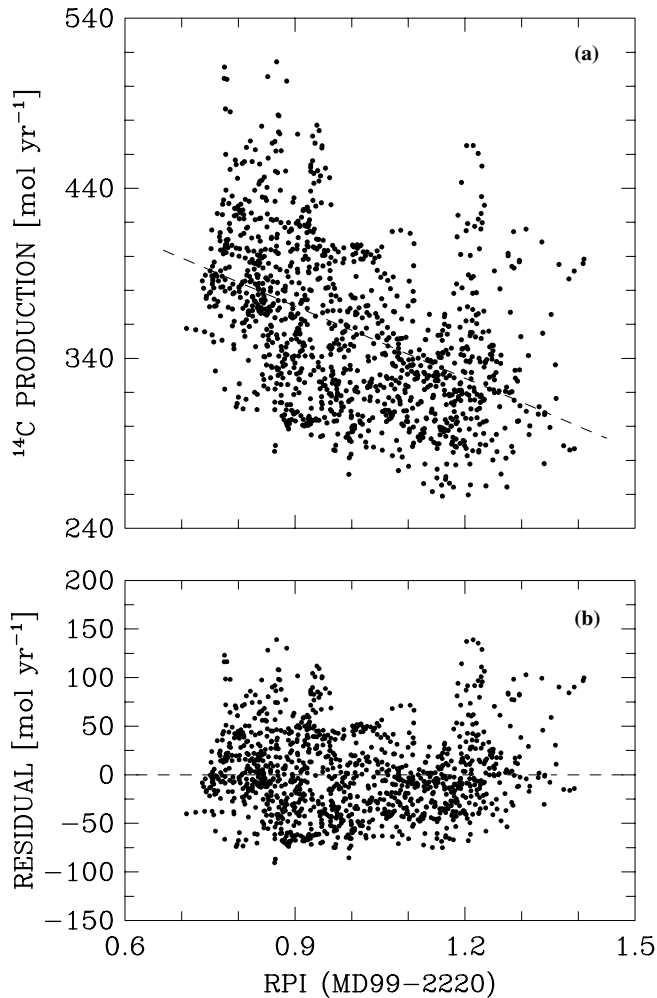


Fig. 9 **a** Scatter plot of the optimal estimates of ^{14}C production versus RPI estimates from magnetic data for sediment core MD99-2220. To avoid congestion the errors in both estimates are not reported. The *dashed line* is the linear regression line. **b** Linear regression residuals (difference between \mathcal{P} and its value on the regression line) versus RPI estimates. The *dashed line* is the zero line (RPI data from St. Onge et al. 2003)

($n = 183$; $p < 0.01$). Thus, approximately 23% of the variance of \mathcal{P} is “explained” by linear regression on GISP2 ^{10}Be data, a linear relationship between both variables being highly significant assuming binormality. The rank correlation coefficient between \mathcal{P} and GISP2 ^{10}Be data amounts to 0.29 ($p < 0.01$), i.e., the two variables show a positive monotonic relationship which is also very significant.

Finally, we compare our best estimates of \mathcal{P} with ^{10}Be concentration data from the PS1 ice core, South Pole (Raisbeck et al. 1990). These data are available only for the recent time interval from AD ~ 750 year onwards, but they occur at a much higher temporal resolution than the GISP2 ^{10}Be data (Fig. 12). Like ^{10}Be concentration in Greenland ice cores, ^{10}Be concentration in PS1 has been assumed to be directly proportional to the global rate of ^{10}Be and ^{14}C production (Bard et al. 1997). The linear regression residuals do not display a clear pattern that

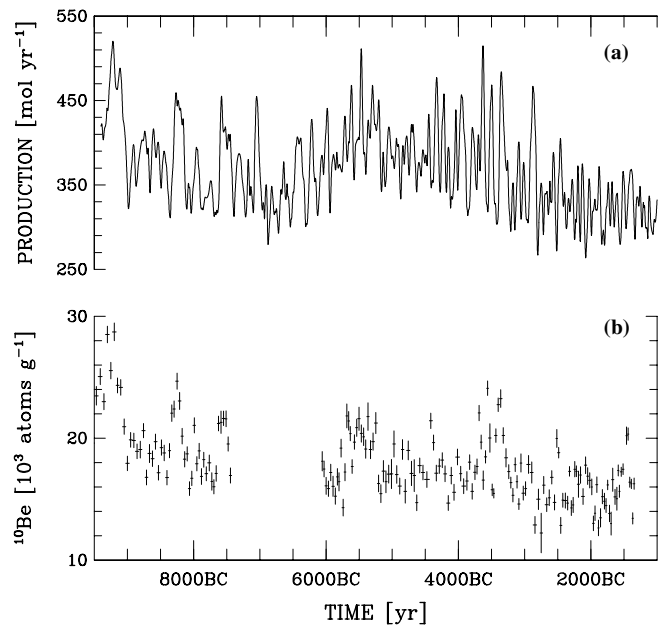


Fig. 10 **a** Optimal estimate of the time evolution of ^{14}C production in the atmosphere. **b** Record of ^{10}Be concentration in the GISP2 ice core, Central Greenland. The *horizontal bars* indicate the time intervals for which ^{10}Be concentration has been measured. The *vertical bars* are the estimated errors in the concentration values (^{10}Be data from Finkel and Nishiizumi 1997; GISP2 time scale of Meese et al. 1994)

would question a linear relation between \mathcal{P} and ^{10}Be concentration in PS1 (Fig. 13b). The linear correlation coefficient between both variables is 0.60 ($n = 133$; $p < 0.01$), i.e., about 36% of the variance in \mathcal{P} is accounted for by linear regression on PS1 ^{10}Be data. Again, a linear relationship would be highly significant assuming binormality. The rank correlation coefficient between \mathcal{P} and ^{10}Be concentration in PS1 is 0.42 ($p < 0.01$), i.e., positive monotonicity is highly significant as well.

In summary, our optimal estimates of atmospheric ^{14}C production inferred from the tree-ring $\Delta^{14}\text{C}$ record correlate strongly with archeomagnetic data and with ^{10}Be concentration data from polar ice cores of both the northern and southern hemisphere (all p values < 0.01). We find, however, that an important fraction of the variance in the paleointensity and ^{10}Be records is not related to ^{14}C production changes as implied by the tree-ring data (42–77% according to the linear regressions). These relatively high fractions of unexplained variance could be due to different causes. For example, it is possible that stronger correlations could be obtained by altering the original chronology of the paleointensity and ^{10}Be records. This exercise is not attempted here. Also, a major source of variability in ^{10}Be concentration records from ice cores is changes in the (snow) accumulation rate (e.g., Yiou et al. 1997), which is not expected to covary with ^{10}Be production in the atmosphere. A more consistent comparison between the ^{10}Be data and our \mathcal{P} estimates should therefore consider the effects of accumulation changes on ^{10}Be concentration.

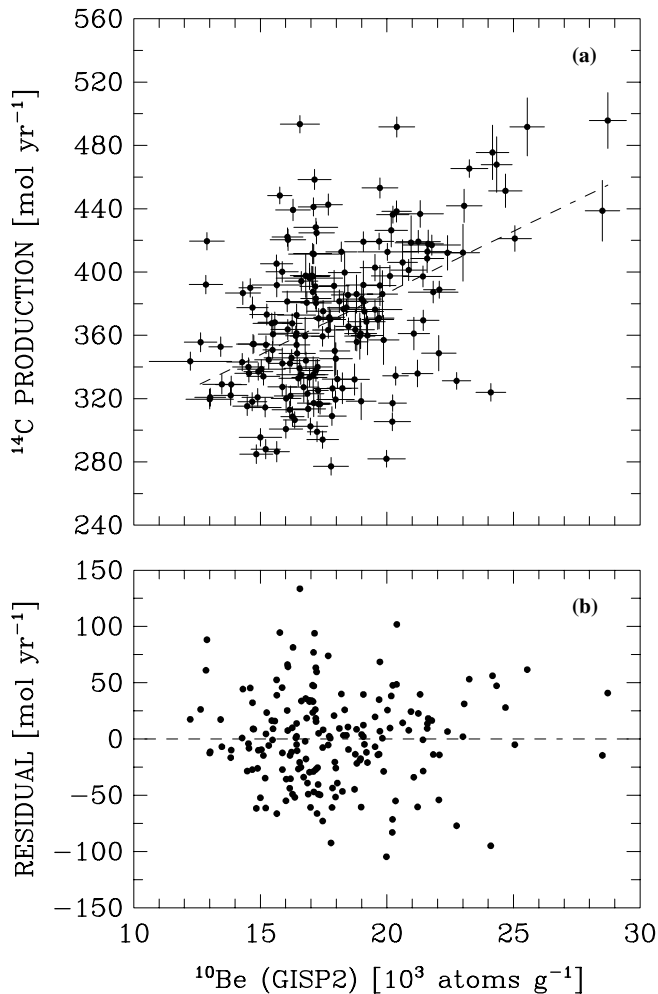


Fig. 11 **a** Scatter plot of the optimal estimates of ^{14}C production versus ^{10}Be concentration data for GISP2 ice core (Central Greenland). The \mathcal{P} values are the averages in the time intervals (ice core section) for which ^{10}Be concentration has been measured. The errors in ^{14}C production estimates (vertical bars) are the errors at the middle of these intervals. The errors in the ^{10}Be concentration data are shown by horizontal bars. The dashed line is the linear regression line. **b** Linear regression residuals (difference between \mathcal{P} and its value on the regression line) versus ^{10}Be concentration data for GISP2. The dashed line is the zero line (^{10}Be data from Finkel and Nishiizumi 1997)

Finkel and Nishiizumi (1997) used one of the three accumulation records calculated by Cuffey and Clow (1997) to estimate ^{10}Be fluxes at GISP2, which should reduce these effects. To test these effects on our results, we compute ^{10}Be fluxes for GISP2 using the accumulation rates calculated by assuming a 100 km retreat of the ice sheet margin during the deglaciation (Cuffey and Clow 1997). We find that both the linear and rank correlations with our \mathcal{P} estimates (coefficients of 0.27 and 0.18, respectively) are actually less when changes in accumulation are not considered (0.48 and 0.29, respectively). Thus, considering accumulation changes does not, at least systematically, improve the correlations with these estimates.

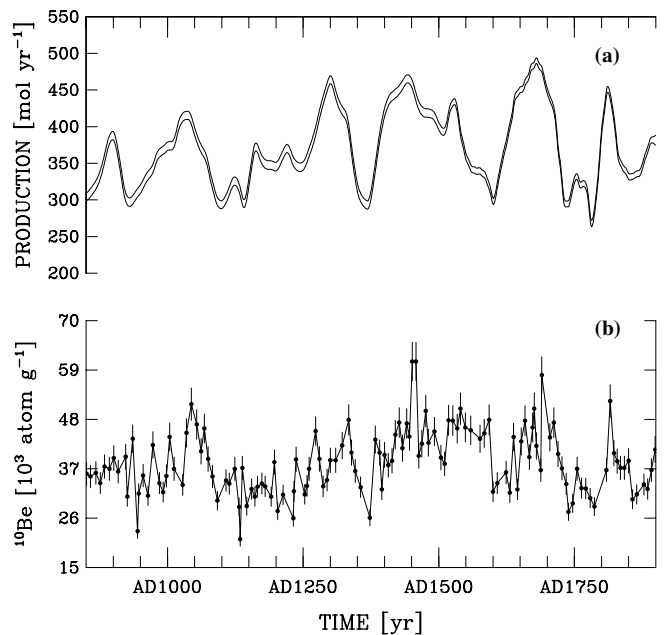


Fig. 12 **a** Optimal estimate of the time evolution of ^{14}C production in the atmosphere. The upper (lower) curve is the optimal estimate plus (minus) its error. **b** Record of ^{10}Be concentration for the PS1 ice core, South Pole (data from Raisbeck et al. 1990). The vertical bars are the estimated errors in the concentration values (7%; Bard et al. 1997)

4.2 Paleoclimate implications

Our best estimate of the time evolution of atmospheric ^{14}C production (Fig. 6) should contain information about the variability in solar activity on time scales >10 yr (the resolution of tree-ring $\Delta^{14}\text{C}$ data) during the Holocene. Our results may therefore give insights into the hypothesized link between variations in solar activity and climate during this period. More specifically, it has been argued that a solar forcing mechanism may underlie at least the Holocene segment of a “1500-year” climate cycle in the North Atlantic (Bond et al. 2001). The argument was based on a comparison between (1) a reconstruction of ^{14}C production from tree-ring $\Delta^{14}\text{C}$ data and a composite record of ^{10}Be flux at Central Greenland with (2) different records of drift ice proxies measured in North Atlantic sediment cores. For the comparison, the \mathcal{P} and ^{10}Be flux records were detrended using a gaussian band-pass filter designed to remove all energy at periods >1800 yr and smoothed using a binomial function with a smoothing window of 70 yr (the mean resolution of the marine records). That is, all components in the records with energy at periods shorter than 1800 yr were considered of solar origin.

We conduct a spectral analysis of our best estimates of ^{14}C production to examine the contention of Bond et al. (2001). These estimates are available on a regular temporal grid (with $\Delta t = 1$ yr), so that data interpolation, which could influence the spectrum estimate (e.g., Yiou et al. 1996), or the use of a relatively sophisticated

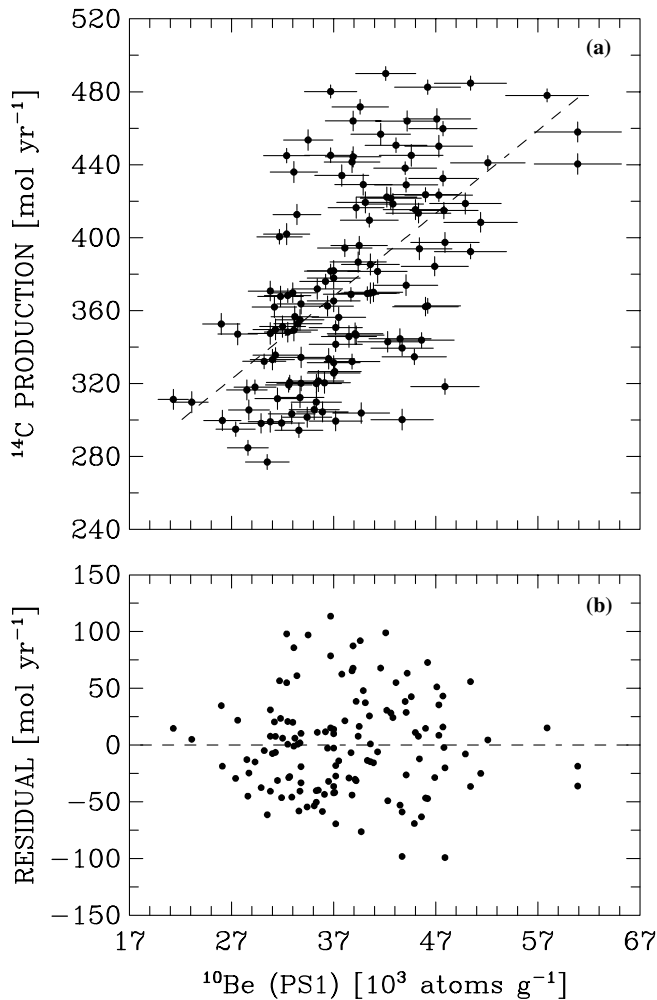


Fig. 13 **a** Scatter plot of the optimal estimates of ^{14}C production versus ^{10}Be concentration data for PS1 ice core (South Pole). The errors in ^{14}C production estimates are shown by vertical bars. The errors in ^{10}Be concentration data are shown by horizontal bars (7%; Bard et al. 1997). The dashed line is the linear regression line. **b** Linear regression residuals (difference between \mathcal{P} and its value on the regression line) versus ^{10}Be concentration data for PS1. The dashed line is the zero line (^{10}Be data from Raisbeck et al. 1990)

method (e.g., Schulz and Stattger 1997) are not necessary. First, we compute the periodogram (Fig. 14a). Although the periodogram is the “natural” estimator of the power spectrum, its poor bias and variance properties imply that it is actually of limited use in estimating this spectrum (e.g., Percival and Wanden 1993). Albeit instructive, it should thus be interpreted with particular caution. The periodogram of our \mathcal{P} estimates is essentially red, with most energy present at low frequencies (by Parseval’s theorem the total area under the periodogram is equal to the total variance or energy in the time series). According to the periodogram, the energy at periods <1800 yr represents 62% of the total energy in the \mathcal{P} estimates. Assuming as Bond et al. (2001) that all the energy at periods <1800 yr is of solar origin, the solar component in these estimates would therefore be dominant. However, the energy in the band 1200–1800 yr

(which is centered at 1500 yr and is taken here as the “millennial band”) amounts to only 0.5% of the total energy and 0.8% of the “solar” energy at periods <1800 yr. Importantly, the band corresponds to a trough, not to a peak, in the periodogram.

A smoothed spectrum calculated so as to reduce the variance of the spectral ordinates may increase the fraction of energy in the millennial band but obviously should not lead to a spectral peak. To produce a power spectrum estimate, we average the spectral ordinates of the periodogram in groups of fixed number m of Fourier frequencies, using in the averages the same weight for each ordinate; the resulting spectrum estimate is identical to the one obtained from the Daniell window with a lag window calculated from the same value of m (e.g., Chatfield 1996). Assuming $m=11$ reduces considerably the variance of the spectrum at most frequencies and the intensity of the trough in the millennial band (Fig. 14b). The energy at periods <1800 yr then represents 68% of the total energy in the \mathcal{P} time series. The energy in the band 1200–1800 yr represents 4% of the total energy and 6% of the “solar” energy at periods <1800 yr. Sensitivity tests show that both fractions remain lower than 15% for a wide range of m values (Fig. 14c).

These results are not consistent with the hypothesis that variations in solar activity contributed to the postulated climate variations at the millennial time scale during the Holocene (e.g., Bond et al. 2001). Confidence in this hypothesis would be increased if it can be demonstrated that cosmogenic nuclide production records contain an energy maximum in the millennial band (consider, e.g., the role played by the “discovery” of Milankovitch frequencies in marine sediment records in promoting an orbital theory of climate change). In contrast, the spectrum of our ^{14}C production estimates near 10^{-3}yr^{-1} frequency corresponds to a trough or is flat, but does definitively not show a peak (Fig. 14a–b). Schulz and Paul (2002) argued that the existing paleoceanographic evidence for ~ 1400 – 1500 yr climate oscillations during the Holocene is actually questionable. They suggested that deep-sea records from the North Atlantic may be reconciled with 900-yr climate oscillations during this period as they found in the GISP2 $\delta^{18}\text{O}$ record. Our \mathcal{P} estimates do not show a peak at this time scale either (Fig. 14b). Sensitivity tests using the same values of m as in Fig. 14c reveal that the energy in the band 800–1000 yr represents 1–8% of the total energy and 1–9% of the “solar” energy at periods <1800 yr. Thus, the existence of a direct solar forcing mechanism for climate oscillations at the ~ 900 -yr time scale is also not supported.

Our results have also some implications regarding claims that changes in solar activity contributed to Holocene climate variability at time scales much shorter than 1500 yr such as the centennial time scales (for recent studies see, e.g., Neff et al. 2001; Fleitmann et al. 2003; Hu et al. 2003). Several studies supported their claim by a cross-spectral analysis of a climate proxy record with a residual $\Delta^{14}\text{C}$ record obtained by removing

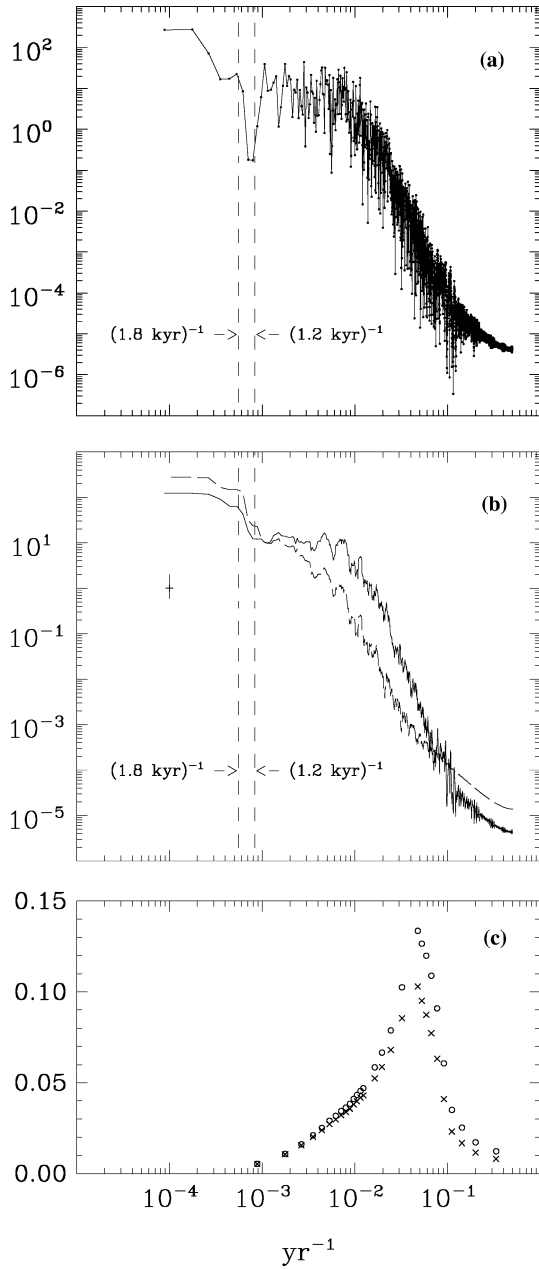


Fig. 14 **a** Raw periodogram of our best ^{14}C production estimates over the Holocene. **b** Smoothed periodogram (power spectrum estimate) of the ^{14}C production values obtained by averaging spectral ordinates in groups of size $m=11$ (solid line) and of the RTS smoother estimates of atmospheric $\Delta^{14}\text{C}$ (linearly detrended values) obtained by averaging spectral ordinates in groups of the same size (dashed line). The criss-cross is the approximate 95% confidence interval for both spectra. In panels (**a**, **b**) the spectral ordinates are normalized to the total power. **c** Ratio (for ^{14}C production) of the power in the band 1200–1800 yr to the total power in the time series (x) and ratio of the power in the band 1200–1800 yr to the total power at periods <1800 yr to the total power at periods <1800 yr (o). For panels (**a**, **b**), the x-axis is frequency, whereas for panel (**c**) it is $(m \Delta t)^{-1}$

some long-term (variable) trend from the tree-ring $\Delta^{14}\text{C}$ data. This approach implies several assumptions—three of them are discussed below. First, it is assumed that the

trend applied to the tree-ring $\Delta^{14}\text{C}$ data captures most of the (unwanted) effects of the changes in the earth magnetic field. There is obviously an infinite number of trends that can be calculated from the original $\Delta^{14}\text{C}$ record, and no guarantee that the selected one best captures these effects. The spectrum of our \mathcal{P} estimates suggests that the variability of ^{14}C production is continuous over a wide range of frequencies (Fig. 14b) and illustrates the difficulty, from knowledge of $\Delta^{14}\text{C}$ data or ^{14}C production estimates only, of separating the effects of the geomagnetic field and solar activity. Second, it is assumed that, when considered in the frequency domain, the residual $\Delta^{14}\text{C}$ record is a reliable analog of a ^{14}C production record. The validity of this assumption is not clear. Even for stable linear systems, the spectrum of the output is not equal to the spectrum of the input (Jenkins and Watts 1968). Consider the power spectrum estimate of atmospheric $\Delta^{14}\text{C}$ in the analysis corresponding to our best \mathcal{P} estimates (dashed line in Fig. 14b). Although the concentration and production spectra show the same overall (red) shape, notable differences are found in the partitioning of total energy between the two time series, particularly near 10^{-2} yr^{-1} frequency. It is probably wise to check that results obtained from cross-spectral analyses are insensitive to the choice of the proxy used for solar activity (e.g., residual $\Delta^{14}\text{C}$ versus ^{14}C production). Finally, the error bars in spectral analyses are based on certain assumptions about the process generating the series; this is true also for relatively sophisticated methods, such as the multitaper (Percival and Walden 1993). It was strongly recommended to apply several independent techniques to test the robustness of spectral results obtained for any time series (Ghil and Yiou 1996). Many procedures of statistical inference assume that the variables have an underlying normal distribution. Several tests of normality exist, which are based on different characteristics of the normal distribution and whose power depends on the nature of the non-normality. The Lilliefors test, for example, is based on the maximum vertical distance between the sample and normal distribution functions (e.g., Dudewicz and Mishra 1988). According to this test, the null hypothesis that our best \mathcal{P} estimates are normal, against the composite hypothesis that they are not, can be rejected at the 1% level. Whereas other normality tests should be used, this suggests that the error bar for the spectrum of our \mathcal{P} estimates (e.g., Fig. 14b) should be interpreted with some caution. Thus, it is probably wise to also examine the distribution of the variables involved before interpreting the error bars in spectral analyses.

In summary, the fundamental difficulty remains, of explaining a peak near 10^{-3} yr^{-1} frequency in the spectrum of climate variability in the absence of a peak in the spectrum of external (orbital) forcing at a similar frequency; the millennial frequency is 5 octaves above the highest Milankovitch frequencies and 5 octaves below the lowest tidal frequencies (Munk et al. 2000). In the absence of a millennial peak in the forcing, the hypotheses to explain climate variability at this time scale

appear relatively sophisticated and speculative. Consider the hypothesis of a solar forcing mechanism. Even if a millennial periodicity in solar (magnetic) activity can be demonstrated, the relation between changes in solar activity and the climatically more relevant changes in solar irradiance (i.e., the integral of the electromagnetic spectrum) on the millennial time scale must be known (for a review of the role of the sun in forcing climate variability, see Beer et al. (2000)). The best constraint on the relation between the two phenomena are for the decadal time scale. During a typical Schwabe cycle, ^{14}C production is estimated from a model to vary by several tens of percents (Masarik and Beer 1999). In contrast, satellite measurements indicate that solar irradiance varied by only $\sim 0.1\%$ during solar cycle 22 (Beer et al. 2000) (for reference, the seasonal variation in solar irradiance outside the atmosphere amounts to $\sim 100\%$ at 45° of latitude). This reminds us of how efficient a possible “amplifier” in the climate system has to be for the changes in solar irradiance per se to affect climate, at least at the decadal time scale.

5 Conclusions

An optimal estimate of the time evolution of ^{14}C production in the atmosphere over the Holocene has been inferred from a combination of a tree-ring $\Delta^{14}\text{C}$ record and a box model of the global ^{14}C cycle. The estimate is optimal in the sense that it is consistent with both the tree-ring data and the model conservation equations within the estimated (supposedly purely random) errors in these data and in these equations. Whereas the estimate is precise, no guarantee can be given as to whether it is also accurate given that systematic errors have not been addressed. Nevertheless, it is thought that our approach provides a more rigorous interpretation, both conceptually and operationally, of the tree-ring $\Delta^{14}\text{C}$ record in terms of production changes than earlier studies. Our optimal estimates of \mathcal{P} show highly significant correlations ($p < 0.01$) with independent evidence of changes in cosmogenic nuclide production in the atmosphere during the Holocene from different archives. However, an important fraction of the variance in data of the geomagnetic field intensity and ice core ^{10}Be concentration (42–77% according to the linear regressions) is not related to the \mathcal{P} changes implied by the tree-ring $\Delta^{14}\text{C}$ data. The \mathcal{P} variance in the millennial band (1200–1800 yr), which some authors interpreted as solar variability, represents a small fraction of the total variance ($< 15\%$) and does not correspond to a spectral peak. Hence, our results do not strengthen the hypothesis that the purported climate variability at the millennial time scale during the Holocene results from a direct forcing by the sun.

Acknowledgements I am strongly indebted to Carl Wunsch for having pointed to the RTS smoother as a possible methodology to solve the present problem of data-model combination. Carl

Wunsch also conducted a multitaper analysis of our production estimates and provided useful comments on different versions of the manuscript. I also thank Peter Huybers and Guillaume St-Onge for comments and Jürg Gasser, Andrew Solow, and Lisan Yu for discussions. Comments by two anonymous reviewers and the editor also improved the manuscript. Richard Alley provided useful information about ice core ^{10}Be data. Finally, I acknowledge different investigators for having supplied data to me. Bill Allan supplied estimates of ^{14}C production during solar cycle 23. Edouard Bard sent me the ^{10}Be data from South Pole. Jozef Masarik provided results from his cosmogenic nuclide production model. Guillaume St-Onge shared his magnetic data for core MD99-2220. This work was supported by the Ocean and Climate Change Institute at WHOI. This is WHOI contribution number 11221.

Appendix 1: RTS methodology

This Appendix describes the RTS methodology used in the paper. The methodology is detailed enough to permit other investigators to repeat the analysis or to use our approach for other problems of a similar nature. More detailed and rigorous accounts can be found in the original reference (Rauch et al. 1965) and in several textbooks of applied optimal estimation (e.g., Meditch 1969; Gelb et al. 1974; Bryson and Ho 1975; Wunsch 1996; Brown and Hwang 1997). The RTS methodology is based on the Kalman filter and the RTS smoother. The Kalman filter assumes a probabilistic description for the measurement error \mathbf{v}_i , the system forcing \mathbf{w}_i , and the initial state \mathbf{x}_0 :

$$E(\mathbf{v}_i) = \mathbf{0} \quad \text{and} \quad E(\mathbf{v}_i \mathbf{v}_j^T) = \mathbf{R}_i \delta_{ij}, \quad (11)$$

$$E(\mathbf{w}_i) = \bar{\mathbf{w}}_i \quad \text{and} \quad E(\mathbf{w}_i - \bar{\mathbf{w}}_i)(\mathbf{w}_j - \bar{\mathbf{w}}_j)^T = \mathbf{Q}_i \delta_{ij}, \quad (12)$$

$$E(\mathbf{x}_0) = \bar{\mathbf{x}}_0 \quad \text{and} \quad E(\mathbf{x}_0 - \bar{\mathbf{x}}_0)(\mathbf{x}_0 - \bar{\mathbf{x}}_0)^T = \bar{\mathbf{P}}_0, \quad (13)$$

where $E(\cdot)$ is the expectation, δ is the Kronecker delta ($\delta_{ij} = 1$ if $i = j$ and $\delta_{ij} = 0$ if $i \neq j$), \mathbf{R}_i is the covariance matrix for the measurement errors, \mathbf{Q}_i is the covariance matrix for the system forcing, and $\bar{\mathbf{P}}_0$ is the covariance matrix for the errors in the initial state. The relations (11) and (12) state that the measurement errors and the system forcing are individually uncorrelated in time. Thus, the sequences $\mathbf{v}_1, \mathbf{v}_2, \dots$ and $\mathbf{w}_0, \mathbf{w}_1, \dots$ are assumed to be purely random sequences (“white sequences”). This implies that the cross-covariances between \mathbf{v}_i , \mathbf{w}_i , and \mathbf{x}_0 also vanish. From assumptions (11), (12) and (13) the Kalman filter estimate of the state \mathbf{x}_i is derived:

$$\bar{\mathbf{x}}_i = \bar{\mathbf{x}}_i + \mathbf{K}_i(\mathbf{z}_i - \mathbf{H}_i \bar{\mathbf{x}}_i), \quad (14)$$

where

$$\bar{\mathbf{x}}_{i+1} = \Phi_i \hat{\mathbf{x}}_i + \Gamma_i \bar{\mathbf{w}}_i, \quad (15)$$

$$\mathbf{K}_i = \hat{\mathbf{P}}_i \mathbf{H}_i^T \mathbf{R}_i^{-1}, \quad (16)$$

$$\hat{\mathbf{P}}_i = \left(\hat{\mathbf{P}}_i^{-1} + \mathbf{H}_i^T \mathbf{R}_i^{-1} \mathbf{H}_i \right)^{-1}, \quad (17)$$

$$\bar{\mathbf{P}}_{i+1} = \Phi_i \hat{\mathbf{P}}_i \Phi_i^T + \Gamma_i \mathbf{Q}_i \Gamma_i^T. \quad (18)$$

The matrix \mathbf{K}_i is the Kalman gain, $\bar{\mathbf{P}}_i = E(\mathbf{x}_i - \bar{\mathbf{x}}_i)(\mathbf{x}_i - \bar{\mathbf{x}}_i)^\top$ is the covariance matrix for the errors in the state estimate prior to measurement $\bar{\mathbf{x}}_i$, and $\hat{\mathbf{P}}_i = E(\mathbf{x}_i - \hat{\mathbf{x}}_i)(\mathbf{x}_i - \hat{\mathbf{x}}_i)^\top$ is the covariance matrix for the errors in the state estimate after measurement $\hat{\mathbf{x}}_i$. The relations (14), (15), (16), (17), (18) all have physical interpretation. The vector difference $\mathbf{z}_i - \mathbf{H}_i\bar{\mathbf{x}}_i$ in relation (14) represents the new information brought about by the measurements. The Kalman gain \mathbf{K}_i is essentially a measure of the ratio between the uncertainty in the state $\bar{\mathbf{P}}_i$ and the uncertainty in the measurements \mathbf{R}_i (relation 16). Relation (14) thus shows that, when the ratio is large, the filter tends to give less weight to the state estimated prior to measurement ($\bar{\mathbf{x}}_i$, calculated using Eq. 15) and more weight to the measurements (\mathbf{z}_i), in estimating the state ($\hat{\mathbf{x}}_i$). As the matrix $\mathbf{H}_i^\top \mathbf{R}_i^{-1} \mathbf{H}_i$ is positive-definite, relation (17) states that, on average, the measurements \mathbf{z}_i decrease the uncertainty in our knowledge of the state \mathbf{x}_i . Similarly, as $\Gamma_i \mathbf{Q}_i \Gamma_i^\top$ is positive semi-definite, Eq. 18 (a covariance propagation equation) shows that, on average, the effect of the uncertainty in \mathbf{w}_i is to increase the uncertainty in our knowledge of \mathbf{x}_i . The effect of $\Phi_i \hat{\mathbf{P}}_i \Phi_i^\top$ in Eq. 18 is less obvious as it depends on the stability of the system, i.e., on the eigenvalues of Φ_i .

In contrast to the Kalman filter, the RTS smoother provides an estimate of \mathbf{x}_i using all the measurements in the sequence $\mathbf{z}_1, \mathbf{z}_2, \dots, \mathbf{z}_N$, where $i < N$. The measurements \mathbf{z}_{i+1} yield information about the state \mathbf{x}_i and about the transition from state i to state $i+1$, i.e., about the forcing \mathbf{w}_i . The smoother therefore permits an estimation of \mathbf{w}_i , as well as of \mathbf{x}_i . We denote the RTS smoother estimate of the state by $\tilde{\mathbf{x}}_i$, of the forcing by $\tilde{\mathbf{w}}_i$, of the covariance matrix for the state errors by $\tilde{\mathbf{P}}_i$, and of the covariance matrix for the forcing by $\tilde{\mathbf{Q}}_i$. The RTS smoother is:

$$\tilde{\mathbf{x}}_i = \hat{\mathbf{x}}_i - \mathbf{C}_i(\bar{\mathbf{x}}_{i+1} - \tilde{\mathbf{x}}_{i+1}), \quad \tilde{\mathbf{x}}_N \equiv \hat{\mathbf{x}}_N, \quad (19)$$

$$\tilde{\mathbf{w}}_i = \bar{\mathbf{w}}_i - \mathbf{B}_i(\bar{\mathbf{x}}_{i+1} - \tilde{\mathbf{x}}_{i+1}), \quad (20)$$

$$\tilde{\mathbf{P}}_i = \hat{\mathbf{P}}_i - \mathbf{C}_i(\bar{\mathbf{P}}_{i+1} - \tilde{\mathbf{P}}_{i+1})\mathbf{C}_i^\top, \quad \tilde{\mathbf{P}}_N \equiv \hat{\mathbf{P}}_N, \quad (21)$$

$$\tilde{\mathbf{Q}}_i = \mathbf{Q}_i - \mathbf{B}_i(\bar{\mathbf{P}}_{i+1} - \tilde{\mathbf{P}}_{i+1})\mathbf{B}_i^\top, \quad (22)$$

where

$$\mathbf{C}_i = \hat{\mathbf{P}}_i \Phi_i^\top \bar{\mathbf{P}}_{i+1}, \quad (23)$$

$$\mathbf{B}_i = \mathbf{Q}_i \Gamma_i^\top \bar{\mathbf{P}}_{i+1}. \quad (24)$$

Thus, to determine the smoother estimates, the Kalman filter estimates $\hat{\mathbf{x}}_i$, $\hat{\mathbf{P}}_i$, and the intermediate quantities \mathbf{x}_i , \mathbf{P}_i must first be calculated. This calculation requires a forward sweep through the measurements \mathbf{z}_i using the relations (14), (15), (16), (17), (18). Since $\tilde{\mathbf{x}}_N \equiv \hat{\mathbf{x}}_N$ and $\tilde{\mathbf{P}}_N \equiv \hat{\mathbf{P}}_N$, the smoother estimates $\tilde{\mathbf{x}}_i$, $\tilde{\mathbf{w}}_i$, $\tilde{\mathbf{P}}_i$, and $\tilde{\mathbf{Q}}_i$ can then be computed through a backward sweep with the recursion relations (19), (20), (21), (22), (23), (24).

Appendix 2: state augmentation

This Appendix describes the state augmentation approach (e.g., Brown and Hwang 1997) that is used to account for the presence of sequential correlation in the system forcing (i.e., in the ^{14}C production variations). As implied by its terminology the approach is based on the addition of one element in the state vector \mathbf{x} . (hence, the addition of a dot subscript to distinguish \mathbf{x} . from the state vector \mathbf{x} , which is of a higher dimension and effectively used in the analysis). First, we assume that a valid probabilistic description of \mathcal{P} is the random walk:

$$\mathcal{P}_{i+1} = \mathcal{P}_i + w_{\mathcal{P},i}, \quad (25)$$

where $E(w_{\mathcal{P},i}) = 0$ and $E(w_{\mathcal{P},i} w_{\mathcal{P},j}) = q_{\mathcal{P}} \delta_{ij}$. The production \mathcal{P}_{i+1} is taken as the sum of the production \mathcal{P}_i at some earlier time and of a stochastic component that has zero mean, constant variance $q_{\mathcal{P}}$, and zero time correlation. By assuming a random walk, we allow the estimated \mathcal{P} to have a variable expectation and variance over the Holocene, i.e., nonstationary features such as “trends” may be present in the estimated time evolution of \mathcal{P} (e.g., Chatfield (1996)). We then define the following quantities in the transition equation $\mathbf{x}_{i+1} = \Phi_i \mathbf{x}_i + \Gamma_i \mathbf{w}_i$ (Eq. 2 in the main text). The state vector \mathbf{x} is augmented to include \mathcal{P} as an additional variable, i.e.,

$$\mathbf{x}^\top = [x_a, x_b, x_d, x_h, x_l, \mathcal{P}]. \quad (26)$$

The transition matrix for the state is a 6×6 partitioned matrix, i.e.,

$$\Phi_i = \begin{bmatrix} \Phi_i & \vdots & \mathbf{1} \\ \dots & \dots & \dots \\ \mathbf{0} & \vdots & \mathbf{1} \end{bmatrix}.$$

The transition matrix for the forcing, Γ_i , is the 6×6 identity matrix. Finally, the forcing \mathbf{w}_i is a 6×1 vector, i.e., $\mathbf{w}_i^\top = [w_{a,i}, w_{b,i}, w_{d,i}, w_{h,i}, w_{l,i}, w_{\mathcal{P},i}]$. The first five elements of \mathbf{w}_i are the stochastic components in the equations for ^{14}C concentration. The sixth element is the stochastic component in the random walk model for ^{14}C production in the atmosphere. Conceptually, the elements of \mathbf{w}_i could be viewed as the model errors.

Appendix 3: a priori statistics

In this Appendix, we describe how the different quantities that must be specified a priori to estimate the time evolution of \mathcal{P} have been determined. Consider first \mathbf{R}_i . Because we dispose of only one record of observations, the matrix \mathbf{R}_i is a scalar, i.e., $\mathbf{R}_i = r_i$. We set $r_i = \sigma_i^2$, where σ_i is $(10^{-3} r^* x_a^*)$ times the reported error in the tree-ring $\Delta^{14}\text{C}$ datum for time t_i (Fig. 1b). Consider then $\hat{\mathbf{x}}(0)$. The first element of $\hat{\mathbf{x}}_0$, i.e., the estimate of the concentration of ^{14}C in the atmosphere at 9400 yr BC ($\hat{x}_{a,0}$), is obtained directly from the tree-ring record using Eq. 4

(Fig. 1a). The second-to-fifth elements of $\hat{\mathbf{x}}_0$, i.e., the estimates of the initial ^{14}C concentration in each of the other reservoirs, are obtained from a steady state solution of the model for which the atmospheric ^{14}C concentration = $\hat{x}_{a,0}$. The sixth element of $\hat{\mathbf{x}}_0$, i.e., the estimate of the initial ^{14}C production in the atmosphere, is then diagnosed from this solution, leading to a value of 420 mol yr^{-1} . For reference, observational studies based on the analysis of the specific activity of ^{14}C and theoretical models led to estimates of the global average ^{14}C production in the modern atmosphere in the range $1.75\text{--}2.02 \text{ atoms cm}^{-2} \text{ s}^{-1}$ (see compilation in Masarik and Beer 1999), i.e., $467\text{--}540 \text{ mol yr}^{-1}$. Whereas our diagnosed values do not have to match these estimates (for example, the model atmosphere has some arbitrary volume, V_a , and the two periods are clearly different), we note the broad agreement between them. Now consider $\hat{\mathbf{P}}_0$. The diagonal elements of $\hat{\mathbf{P}}_0$ are the expected values of $(x_{k,0} - \hat{x}_{k,0})^2$, where $k \in \{a, b, d, h, l, \mathcal{P}\}$. The first diagonal element, noted $\hat{p}_{a,0} = E(x_{a,0} - \hat{x}_{a,0})^2$, is set equal to r_0 . For the other diagonal elements, we assume that the uncertainty of the estimated state variable at 9400 yr BC scales as the uncertainty in the tree-ring datum for this time, i.e., $\hat{p}_{k,0} = \hat{p}_{a,0}(\hat{x}_{k,0}/\hat{x}_{a,0})^2$, where $k \in \{b, d, h, l, \mathcal{P}\}$. For simplicity, we assume that the off-diagonal elements of $\hat{\mathbf{P}}_0$ vanish, i.e., $\hat{\mathbf{P}}_0$ is a diagonal matrix, which we write as $\hat{\mathbf{P}}_0 = \text{diag}[\hat{p}_{a,0}, \hat{p}_{b,0}, \hat{p}_{d,0}, \hat{p}_{h,0}, \hat{p}_{l,0}, \hat{p}_{\mathcal{P},0}]$. The sensitivity of our results to the diagonal elements of $\hat{\mathbf{P}}_0$ are explored in Sect. 3.3.

Finally, the covariance matrix for the model errors \mathbf{Q}_i must also be prescribed. A sensible approach is to assume that \mathbf{Q}_i is constant and diagonal, i.e., $\mathbf{Q}_i = \mathbf{Q} = \text{diag}[q_a, q_b, q_d, q_h, q_l, q_{\mathcal{P}}]$, where q_k is the variance of the stochastic component for state variable k (in units $(\text{mol m}^{-3})^2$). On the other hand, the prescription of a positive value for each diagonal element of \mathbf{Q} is motivated both conceptually (the model is not exact) and computationally (Brown and Hwang 1997). Consider first $q_{\mathcal{P}}$, which dictates the amount by which ^{14}C production can change from one discrete time to the next in the random walk model (Eq. 25). The choice of $q_{\mathcal{P}}$ can be guided by physical considerations and/or by statistical considerations about some diagnostics of the Kalman filter and RTS smoother. An important contributor to the year-to-year variation in the production of cosmogenic nuclides in the atmosphere is the 11-yr (Schwabe) cycle in the solar activity (Masarik and Beer 1999). These authors used a cosmogenic nuclide production model to simulate the variations of \mathcal{P} during a “typical” cycle. In their model, the global production rate \mathcal{P} during the solar minimum (maximum) is 1.19 (0.82) times the average rate over a complete solar cycle (Masarik and Beer 1999; p 12, 107). Approximating the change in \mathcal{P} as the function $A \cos(\omega t)$, where A is the amplitude and $\omega = 2\pi / 11 \text{ yr}^{-1}$ is the angular frequency, the variance of \mathcal{P} during one half of the cycle is equal to $A^2/2$, and the corresponding standard deviation = 13% of the average production. The production deviation would then

amount to $61\text{--}70 \text{ mol yr}^{-1}$, where the range reflects the different estimates of the modern global production reported above. Our analysis, on the other hand, is based on decadal averages of $\Delta^{14}\text{C}$ data. Thus, the amount by which \mathcal{P} should change from one time to the next in the random walk model should be lower than the above estimates of the production deviation associated with the 11-yr solar cycle. In our study, we test different values of $V_a/\Delta t\sqrt{q_{\mathcal{P}}}$ which are lower than these estimates and constrain the “best” value from diagnostics of the analysis (Sect. 3.1). With the values of $q_{\mathcal{P}}$ tested in this study, we have not encountered any computational problem in assuming q_a, q_b, q_d, q_h , and q_l all set to zero. For simplicity, these five variances will therefore be set to zero. The sensitivity of our results to different values of q_k , where $k \in \{a, b, d, h, l\}$, are explored as well (Sect. 3.3).

References

- Bard E, Raisbeck GM, Yiou F, Jouzel J (1997) Solar modulation of cosmogenic nuclide production over the last millennium: comparison between ^{14}C and ^{10}Be records. *Earth Planet Sci Lett* 150:453–462
- Beer J, Siegenthaler U, Bonani G, Finkel RC, Oeschger H, Suter M, Wölfli W (1988) Information on past solar activity and geomagnetism from ^{10}Be in the Camp Century ice core. *Nature* 331:675–679
- Beer J, Mende W, Stellmacher R (2000) The role of the sun in climate forcing. *Quat Sci Rev* 19:403–415
- Bond G, Kromer B, Beer J, Muscheler R, MN Evans, Showers W, Hoffmann S, Lotti-Bond R, Hajdas I, Bonani G (2001) Persistent solar influence on North Atlantic climate during the Holocene. *Science* 294:2130–2136
- Brown PG, Hwang PYC (1997) Introduction to random signals and applied Kalman filtering, 3rd edn. Wiley, New York, p 484
- Brownlee KA (1965) Statistical theory and methodology in science and engineering. Wiley series in probability and mathematical statistics. Wiley, New York, p 590
- Bryson AE, Ho Y-C (1975) Applied optimal control: optimization, estimation, and control. Taylor and Francis, Hemisphere Publishing Corporation, p 481
- Chatfield C (1996) The analysis of time series: an introduction. Texts in statistical science. Chapman and Hall/CRC, Boca Raton, p 283
- Cuffey KM, Clow GD (1997) Temperature, accumulation, and ice sheet elevation in central Greenland through the last deglacial transition. *J Geophys Res* 102:26383–26396
- Dudewicz EJ, Mishra SN (1988) Modern mathematical statistics. Wiley series in probability and mathematical statistics. Wiley, New York, p 838
- Finkel RC, Nishiizumi K (1997) Beryllium-10 concentrations in the Greenland Ice Sheet Project 2 ice core from 3–40 ka. *J Geophys Res* 102:26699–26706
- Fleitmann D, Burns SJ, Mudelsee M, Neff U, Kramers J, Mangini A, Matter A (2003) Holocene forcing of the Indian monsoon recorded in a stalagmite from Southern Oman. *Science* 300:1737–1739
- Flückiger J, Monnin E, Stauffer B, Schwander J, Stocker TF (2002) High-resolution Holocene N_2O ice core record and its relationship with CH_4 and CO_2 . *Global Biogeochem Cycles* 16. DOI 10.29/2001GB0001417
- Frank M (2000) Comparison of cosmogenic radionuclide production and geomagnetic field intensity over the last 200,000 years. *Phil Trans Roy Soc Lond A* 358:1089–1107
- Gelb A, Kasper JF, Nash RA, Price CF, Sutherland AA (1974) Applied optimal estimation. MIT Press, p 374

- Ghil M, Yiou P (1996) Spectral methods: What they can do and cannot do for climatic time series. In: Anderson DLT, Willebrand J (eds) Decadal climate variability. Springer, Berlin Heidelberg New York, NATO ASI Series, pp 445–482
- Hu FS, Kaufman D, Yoneji S, Nelson D, Shemesh A, Huang Y, Tian J, Bond G, Clegg B, Brown T (2003) Cyclic variation and solar forcing of Holocene climate in the Alaskan subarctic. *Science* 301:1890–1893
- IPCC (2001) Climate Change 2001. The scientific basis, Contribution of working group I to the 3rd assessment of the Intergovernmental Panel on Climate Change. Cambridge University Press, Cambridge, p 881
- Jenkins GM, Watts DG (1968) Spectral analysis and its applications. Holden-Day, San Francisco, p 525
- Kendall MG, Gibbons JD (1990) Rank correlation methods, 5th edn. Oxford University Press, New York, p 237
- Lasaga AC (1980) The kinetic treatment of geochemical cycles. *Geochim Cosmochim Acta* 44:815–828
- Legrand P, Alverson K (2001) Variations in atmospheric CO_2 during glacial cycles from an inverse ocean modeling perspective. *Paleoceanography* 16:604–616
- Levitus S (1982) Climatological atlas of the world ocean. Technical Report NOAA Prof Pap 13, US Govt Print Office, Washington, p 173
- Luenberger DG (1979) Introduction to dynamic systems—theory, models, and applications. Wiley, New York, p 446
- Masarik J, Beer J (1999) Simulation of particle fluxes and cosmogenic nuclide production in the Earth's atmosphere. *J Geophys Res* 104:12099–12111
- McElhinny MW, Senanayake WE (1982) Variations in the geomagnetic dipole, 1 the past 50,000 years. *J Geomag Geoelectr* 34:39–51
- Meditch JS (1969) Stochastic optimal linear estimation and control. McGraw-Hill, New York, p 394
- Meese DA, Alley RB, Gow AJ, Grootes PM, Mayewski PA, Ram M, Taylor KC, Waddington IE, Zielinski GA (1994) Preliminary depth-age scale of the GISP2 ice core. *Spec Rep 94-I*, Col Reg Res and Eng Lab, Hanover
- Mehra RK (1970) On the identification of variances and adaptive Kalman filtering. *IEEE Trans Automat Contr* 15:175–184
- Munk W, Dzieciuch M, Jayne S (2000) Millennial climate variability: is there a tidal connection. *J Clim* 15:370–385
- Neff U, Burns SJ, Mangini A, Mudelsee M, Fleitmann D, Matter A (2001) Strong coherence between solar variability and the monsoon in Oman between 9 and 6 kyr ago. *Nature* 411:290–293
- Percival DB, Walden AT (1993) Spectral analysis for physical applications—multitaper and conventional univariate techniques. Cambridge University Press, Cambridge, p 583
- Raisbeck GM, Yiou F, Jouzel J, Petit JR (1990) ^{10}Be and $\delta^2\text{H}$ in polar ice cores as a probe of the solar variability's influence on climate. *Phil Trans Roy Soc Lond A* 330:463–470
- Rauch HE, Tung F, Striebel CT (1965) Maximum likelihood estimates of linear dynamics systems. *AIAA J* 3:1445–1450
- Sarmiento JL, Toggweiler JR (1984) A new model for the role of the oceans in determining atmospheric pCO_2 . *Nature* 308:621–624
- Schulz M, Paul A (2002) Holocene climate variability on centennial-to-millennial time scales: 1 Climate records from the North Atlantic realm. In: Wefer G, Berger W, Behre K-E, Jansen E (eds) Climate development and history of the North Atlantic realm. Springer, Berlin Heidelberg New York, pp 41–54
- Schulz M, Statterger K (1997) SPECTRUM: spectral analysis of unevenly spaced paleoclimatic time series. *Comput Geosc* 23:929–945
- Siegenthaler U, Wenk T (1984) Rapid atmospheric CO_2 variations and ocean circulation. *Nature* 308:624–626
- St. Onge G, Stoner JS, Hillaire-Marcel C (2003) Holocene paleomagnetic records from the St. Lawrence Estuary, eastern Canada: Centennial- to millennial-scale geomagnetic modulation of cosmogenic isotopes. *Earth Planet Sci Lett* 209:113–130
- Stocker TF, Wright DG (1996) Rapid changes in ocean circulation and atmospheric radiocarbon. *Paleoceanography* 11:773–796
- Stuiver M, Braziunas TF (1989) Atmospheric ^{14}C and century-scale solar oscillations. *Nature* 338:405–408
- Stuiver M, Braziunas T (1993a) Sun, ocean, climate and atmospheric $^{14}\text{CO}_2$: an evaluation of causal and spectral relationships. *The Holocene* 3:289–305
- Stuiver M, Braziunas TF (1993b) Modeling atmospheric ^{14}C influences and ^{14}C ages of marine samples to 10,000 bc. *Radiocarbon* 35:137–189
- Stuiver M, Braziunas T, Becker B, Kromer B (1991) Climatic, solar, oceanic, and geomagnetic influences on late-glacial and Holocene atmospheric $^{14}\text{C}/^{12}\text{C}$ change. *Quat Res* 35:1–24
- Stuiver M, Reimer PJ, Bard E, Beck W, Burr GS, Hughen KA, Kromer B, McCormac G, van der Plicht J, Spurk M (1998) Intcal98 radiocarbon age calibration, 24,000-0 cal B.P. *Radiocarbon* 40:1041–1083
- Sverdrup HU, Johnson MW, Fleming RH (1942) The Oceans: their physics, chemistry and general biology. Prentice-Hall, Englewood Cliffs, p 1087
- Toggweiler JR (1999) Variation of atmospheric CO_2 by ventilation of the ocean's deepest water. *Paleoceanography* 14:571–588
- Toggweiler J, Sarmiento JL (1985) Glacial to interglacial changes in atmospheric carbon dioxide: the critical role of ocean surface water in high latitudes. In: Sundquist ET, Broecker WS (eds) The carbon cycle and atmospheric CO_2 : natural variations Archean to Present. Geophys Monograph Series, vol 55. AGU, Washington, pp 163–184
- Trudinger CM, Enting IG, Rayner PJ (2002a) Kalman filter analysis of ice core data: 1. Method development and testing the statistics. *J Geophys Res* 107(D20):4422. DOI 10.1029/2001JD001111
- Trudinger CM, Enting IG, Rayner PJ, Francey RJ (2002b) Kalman filter analysis of ice core data: 2. Double deconvolution of CO_2 and $\delta^{13}\text{C}$ measurements. *J Geophys Res* 107(D20):4423. DOI 10.1029/2001JD001112, 2002b
- Wunsch C (1996) The ocean circulation inverse problem. Cambridge University Press, Cambridge, p 442
- Yang S, Odah H, Shaw J (2000) Variations in the geomagnetic dipole moment over the last 12,000 years. *Geophys J Int* 140:158–162
- Yiou P, Baert E, Loutre MF (1996) Spectral analysis of climate data. *Surv Geophys* 17:619–663
- Yiou F, Raisbeck GM, Baumgartner S, Beer J, Hammer C, Johnsen S, Jouzel J, Kubik PW, Lestringuez J, Stiévenard M, Suter M, Yiou P (1997) Beryllium 10 in the Greenland Ice Core Project ice core at Summit, Greenland. *J Geophys Res* 102:26783–26794